Atomically dispersed Co_2-N_6 and Fe-N_4 co-structures boost oxygen reduction reaction in both alkaline and acidic media

Zhe Wang, Xiaoyan Jin, Chao Zhu, Yipu Liu, Hua Tan, Ruiqi Ku, Yongqi Zhang, Liujiang Zhou, Zheng Liu, Seong-Ju Hwang,* Hong Jin Fan**

Dr. Z. Wang, Dr. Y. Liu, Dr. H. Tan, Prof. H. J. Fan
School of Physical and Mathematical Sciences, Nanyang Technological University, 21 Nanyang Link, 637371, Singapore
E-mail: fanhj@ntu.edu.sg

Dr. Z. Wang, Dr. C. Zhu, Prof. Z. Liu
School of Materials Science and Engineering, Nanyang Technological University, 50 Nanyang Avenue, 639798, Singapore

Dr. X. Jin, Prof. S.-J. Hwang
Department of Materials Science and Engineering, Yonsei University, Seoul 03722, Republic of Korea
E-mail: hwangsju@yonsei.ac.kr

R. Ku, Prof. Y. Zhang, Prof. L. Zhou
Institute of Fundamental and Frontier Sciences, University of Electronic Science and Technology of China, Chengdu 610054, China.
E-mail: ljzhou86@uestc.edu.cn

Prof. Y. Zhang, Prof. L. Zhou
Yangtze Delta Region Institute (Huzhou), University of Electronic Science and Technology of China, Huzhou 313001, China.

Keywords: Single atom catalyst, ternary atom sites, oxygen reduction reaction, metal-air batteries, synergistic effect

Abstract

Polynary transition-metal atom catalysts are promising to supersede platinum (Pt)-based catalysts for oxygen reduction reaction (ORR). Regulating the local configuration of atomic catalysts is the key to catalyst performance enhancement. Different from the previously reported single-atom or dual-atom configurations, we develop a new type of ternary-atom catalyst, which consists of atomically dispersed, nitrogen-coordinated Co-Co dimers and Fe single sites (i.e., Co_2-N_6 and Fe-N_4 structures) that are co-anchored on highly graphitized carbon supports. This unique atomic ORR catalyst outperforms the catalysts with only Co_2-N_6 or Fe-N_4 sites in both alkaline and acid conditions. Density functional theory calculations clearly unravels the synergistic effect of the Co_2-N_6 and Fe-N_4 sites, which can induce higher filling degree of Fe-d orbitals and favors the binding capability to *OH intermediates (the rate determining step). This ternary-atom catalyst might be a promising alternative to Pt to drive the cathodic ORR in zinc-air batteries.

The efficient proton exchange membrane fuel cells and rechargeable metal-air batteries, which rely heavily on electrocatalysts for the oxygen reduction reaction (ORR), are considered as promising clean energy candidates for electric vehicles.[1] However, the sluggish kinetics of the cathodic electrochemical ORR severely impede the industrial implementation of these energy techniques.[2] While platinum (Pt)-based materials have served as benchmark electrocatalysts with low overpotential for ORR, the high cost, natural scarcity, and the explicitly correlating methanol crossover to Pt poisoning have limited their large-scale application.[3] Therefore, identifying high-efficiency and cost-effective Pt-free electrocatalysts for ORR has been the focus of recent research in renewable energy.

The key to achieving efficient alternative to Pt-based catalysts is to enhance the intrinsic ORR catalytic activity of specific active sites, and optimize morphological structure to facilitate active sites accessible and mass transfer.[4] Recently, single-atom catalysts (SACs), which contain dispersed metal atoms immobilized on a substrate, are particularly interesting due to their high material utilization efficiency and startling catalytic activity.[5] So far, carbon-supported transition metal (Fe, Co, Mn, Cu etc.) SACs, especially atomically dispersed Fe-N-C and Co-N-C moieties, are being widely investigated and have been proved highly active for ORR.[1c, 6] However, their performance is still lagging behind the apex of the M-N-C Volcano plot. Recent studies have demonstrated that the catalytic performance of such SACs can be further enhanced by rationally tailoring center metal atoms (e.g. dual-atom catalysts with

interacted bi-atomic metal cores)[7] and coordination environment (e.g. the adjacent coordination dopants N, O, S, P, etc. and coordination numbers).[8] The optimized geometry and electronic structure of the M-N-C moieties are believed to be directly correlated with O-O bond breaking, and the adsorption/deposition free energies of the relevant oxygen intermediates. Hence, a fine control of the bonding nature of these moieties are effective in enhancing the intrinsic activity for ORR.[4, 9] In particular, the dual-atom catalysts (such as Fe-N_4/Ni-N_4) have shown enhanced catalytic activity compared to mono atoms.[7a, 7f, 10] However, ternary-atom ORR catalysts with three metal cores (i.e., Co_2-N_6/Fe-N_4) as well as the associated catalytic mechanism have not been well elucidated so far.

Herein, we report a facile strategy to achieve ternary-atom catalysts comprised of atomically dispersed and nitrogen-coordinated Co-Co and Fe sites on a CNTs-grafted hollow carbon nanocage (Co_2/Fe-N@CHC). The nature of Co_2/Fe-N sites, where two interlinked Co atoms are to first bond the N ligands and one Fe atom is to first bond the N ligands, forming a local paired configuration as confirmed by synchrotron X-ray absorption and density functional theory (DFT) calculations. It is revealed that the Co_2/Fe-N_{10} centered sites have higher intrinsic ORR activity than the Co_2-N_6 and Fe-N_4 moieties, which can be attributed to the tailored electronic structure of Fe center that weakens the binding capability to O-containing intermediates of the rate determining step. Electrochemistry tests show our Co_2/Fe-N@CHC catalyst exhibits ORR activity that is superior to that of the benchmark Pt/C. Specifically, a positive half-wave potential of 0.915 V (vs. RHE), remarkable stability with 91.1% of initial current retained over 100 hours, and good methanol tolerance in alkaline medium have been obtained. The ORR performance of the Co_2-N_6 and Fe-N_4 pairs in acidic electrolyte is also significantly enhanced. Moreover, to demonstrate the device application, zinc-air batteries based on the Co_2/Fe-N@CHC cathode exhibit a high power density of 232.4 mW cm^{-2} and good cycling stability. Our novel type of transition-metal atom pairs anchored on highly conductive graphitic surface and hierarchical hollow carbon host, as well as the facile synthesis from cheap ZIF-8 templates, make this catalyst material highly promising for application in energy storage and conversion.

Catalyst synthesis and characterization

The strategy for the synthesis of atomically dispersed and nitrogen-coordinated Co_2-Fe ternary-atom centered sites anchored on carbon nanotubes (CNTs)-grafted hollow carbon (Co_2/Fe-N@CHC) is illustrated in **Figure. 1a**. Briefly, zeolitic imidazolate framework-8 (ZIF-8) nanoparticles (NPs) were dissolved in an alkaline Tris buffer. Then an aqueous solution containing dopamine, as well as cobalt and iron salts, was added into above mixture. During

the magnetic stirring in air, the dopamine monomers were self-polymerized to form polydopamine (PDA) around ZIF-8 NPs. Since PDA has a large number of –OH and nitrogen containing functional groups,[11] Co and Fe cations could be linked to such kind of functional groups through covalent bonds or electrostatic attraction, which allows the formation of metal-PDA. Meanwhile, some Co-ions and Fe-ions were reduced to metallic NPs during the polymerization, which then anchored onto the PDA shell that uniformly covered all over the ZIF-8 (Figure S1, Supporting Information). Furthermore, some coordination complexes of ZIF-8 would release organic ligands to produce the pores and provide Zn-ions to coordinate with PDA, while some Zn-ions in ZIF-8 may exchange with Co/Fe-ions in the Co/Fe-rich environment. Thereafter, a highly porous CoFe-PDA@ZIF-8 was obtained (Figure S1, Supporting Information). Meanwhile, the CoFe-PDA@ZIF-8 well maintains the crystalline texture of the ZIF-8, as confirmed by X-ray diffraction (XRD) patterns and Fourier transform infrared attenuated (FTIR) spectra (Figure S2, Supporting Information). After annealing in the presence of melamine at 920 °C in argon atmosphere, Zn species were volatilized, which led to the formation of nanopores. ZIF-8 frameworks were carbonized and converted into hollow carbon architectures simultaneously, and melamine acted as the carbon source for the in-situ growth of CNTs, catalyzed by Co/Fe species. In the last step, acid leaching treatment was employed to remove Co/Fe NPs, and Co_2/Fe-N@CHC were finally obtained after washing and drying.

The morphology of Co_2/Fe-N@CHC was characterized by scanning electron microscopy (SEM) and transmission electron microscopy (TEM) (**Figure 1b** and Figure S3, Supporting Information). Clearly, Co_2/Fe-N@CHC exhibits a well-defined hierarchical architecture, in which dense CNTs extend out the hollow carbon nanocage. Similar morphology is also observed in CoFe NPs@CHC (Figure S4, Supporting Information). According to the high-resolution TEM (HRTEM) images of Co_2/Fe-N@CHC (**Figure 1c** and Figure S5, Supporting Information), the core carbon has a rough and porous structure (due to the evaporation of Zn) and covered by a few layers of highly graphited carbon. Meanwhile, the CNTs with hollow graphene spheres are grafted on the carbon surface, implying good electronic conductivity and thus accelerating the catalytic reactions. N_2 adsorption/desorption isotherms reveals a large Brunauer-Emmett-Teller (BET) surface area of 553.9 $m^2 g^{-1}$ and a highly open porous structure of Co_2/Fe-N@CHC (Figure S6, Supporting Information). Such a hollow carbon nanocage with highly porous structure are conducive to exposing more active sites to the accessible reactive species and provide efficient channels for mass transport. Moreover, no metallic particles or small clusters are observed in the HRTEM images, as also confirmed by the selected area

electron diffraction (SAED) pattern (inset in **Figure 1c**). The powder X-ray diffraction (XRD) pattern of Co_2Fe-N/CHC shows only two broad peaks at approximately 26.2° and 43.3° due to (002) and (101) planes of graphitic carbon (Figure S7, Supporting Information). No peaks of crystalline metallic Co and/or Fe species are detected. High angle annular dark field scanning TEM (HADDF-STEM) image in **Figure 1d** confirms the generic hollow structure of Co_2/Fe-N@CHC. The atomic dispersion of Co/Fe anchored on the N-doped porous carbon host can be directly observed using aberration-corrected (AC) HAADF-STEM, which has been proven a potent and effective tool for verifying single metal atoms. Shown in **Figures 1e-g** are representative images taken from different parts of the sample, i.e., porous carbon core, the highly graphitized edges, and bamboo-like CNTs. The bright spots corresponding to metal atoms (Co or Fe atoms), illustrating a high density of Co and Fe atoms uniformly dispersed across/within the entire carbon host. For the nanoparticle-based samples (CoFe NPs@CHC), in contrast, metallic NPs and nanoclusters embedded in CNTs are both observed along with the single metal atoms, and the C, N, Co, Fe, and very few Zn species are evenly distributed on the hollow carbon nanocages (Figure S8, Supporting Information). The magnified AC HAADF-STEM images of Co_2/Fe-N@CHC (**Figure 1h** and Figure S9, Supporting Information) clearly show paired bright spots in addition to some individual bright spots. The atomic-resolution electron energy-loss spectroscopy (EELS) of Co_2/Fe-N@CHC (**Figure 1i**), recorded from the paired bright spots in the inset STEM image, further corroborates the existence of Co-Co dimers. Meanwhile, the individual bright spots as indicated in the inset STEM image (**Figure 1j**) are identified as Fe atoms. In addition, the presence of Co, Fe, and N elements in the EELS of an extended local area (Figure S10, Supporting Information) suggests that the Co dimers and single Fe atoms are coordinated with N species. The HADDF-STEM image and corresponding X-ray spectroscopic (EDS) mapping of Co_2/Fe-N@CHC (Figure S11, Supporting Information) confirms the homogenous distribution of C, N, Co, and Fe elements over the hollow carbons. Similar homogeneous distribution of elements is also observed in other control samples of Co or Fe single atoms, namely, Co_2-N@CHC and Fe-N@CHC (Figures S12-15, Supporting Information). Meanwhile, N-doped hollow carbon nanocage (NHC) and the pyrolyzed ZIF-8 were also prepared (Figures S14, 15, Supporting Information).

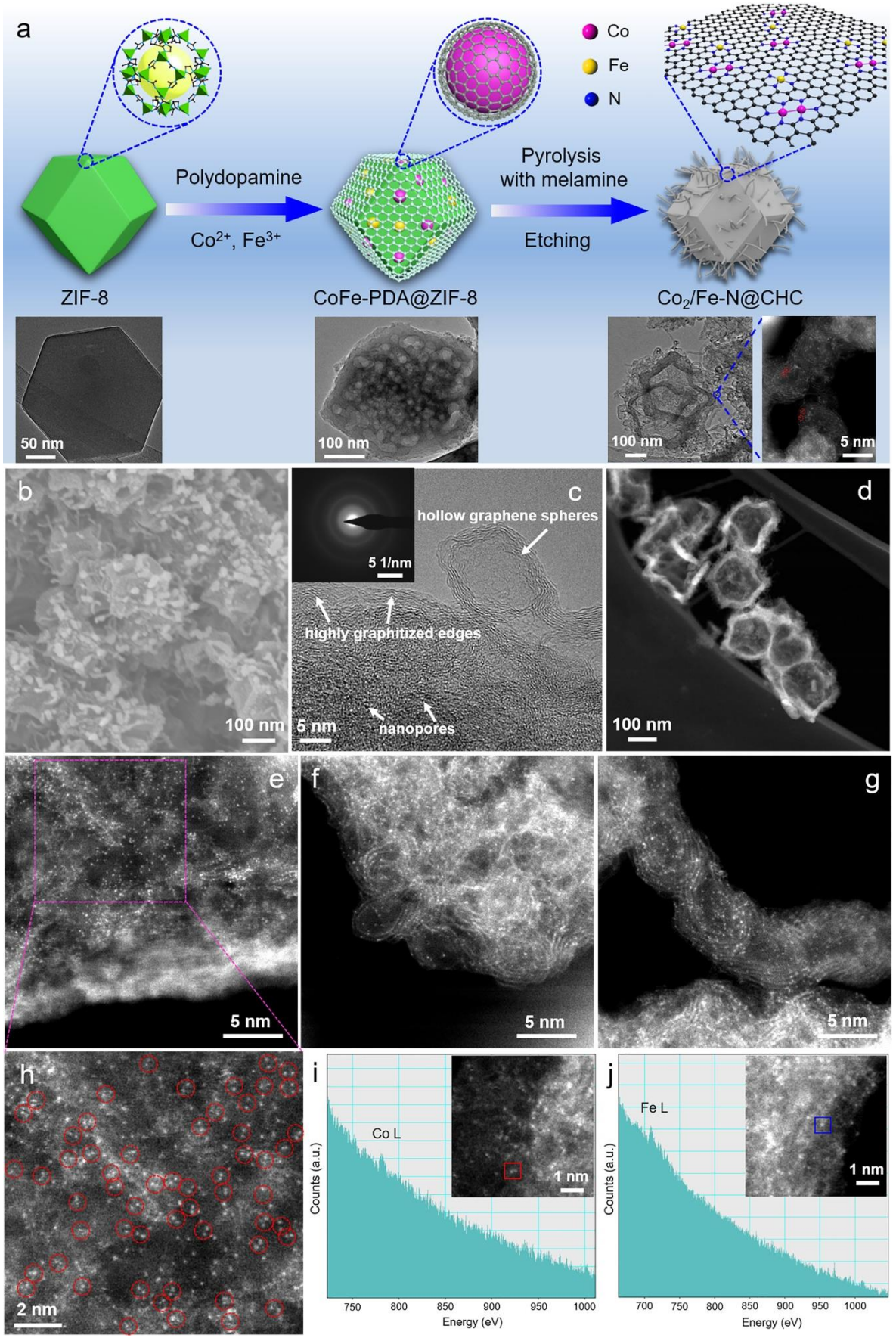

Figure 1. Synthetic strategy and structural characterization of Co_2/Fe-N@CHC. (a) Schematic of the synthesis strategy of Co_2/Fe-N@CHC and corresponding TEM images. (b) SEM image, (c) HRTEM

image, (d) HAADF-STEM image, (e, f, g, h) aberration-corrected HAADF-STEM images of Co_2/Fe-N@CHC. Dashed circles in (h) highlight the paired bright spots. (i, j) EELS analysis of the selected paired spot and single spot in the inset HAADF-STEM images of Co_2/Fe-N@CHC.

Identification of atomic structure

X-ray photoelectron spectroscopy (XPS) was adopted to investigate the surface chemical composition and structure of the as-prepared catalysts. Signals for C, N, Co, and Fe elements are observed in the XPS survey spectrum of Co_2/Fe-N@CHC (Figure S16, Supporting Information), consistent with the EDS elemental mapping. The atomic concentrations of Co and Fe in Co_2/Fe-N@CHC determined by XPS are 0.41 and 0.19 atomic %, respectively, which are close to the inductively coupled plasma-optical emission spectrometry (ICP-OES) results (Table S1, Supporting Information), corresponding to a Co/Fe mole ratio of 2.0. The C 1s XPS spectra exhibit three peaks at binding energies of 284.6, 285.8, and 287.7 eV, corresponding to C-C, C-N, and C-O bonds, respectively (Figure S17, Supporting Information). The high-resolution N 1s spectra are deconvoluted into four characteristic peaks of pyridinic N (398.3 eV), Co/Fe-N (399.4 eV), pyrrolic N (400.2 eV), and graphitic N (401.1 eV) (**Figure 2a**), demonstrating the presence of Co/Fe-N moieties in Co_2/Fe-N@CHC.[12] The Co 2p and Fe 2p spectra of Co_2/Fe-N@CHC reveal the positively charged state of the metal species (Figure S18, Supporting Information). Notably, no zero-valent elemental cobalt and iron species were detected, indicating that the Co and Fe atoms are mostly coordinated with the surrounding atoms.

To further investigate the chemical state and coordination environment of Co and Fe species in Co_2/Fe-N@CHC, X-ray absorption near-edge structure (XANES) and extended X-ray absorption fine structure (EXAFS) spectroscopic analyses were conducted. As shown in the Co K-edge XANES spectra (**Figure 2b**), the position of the absorption threshold for Co_2/Fe-N@CHC is located between those for Co foil and cobalt phthalocyanine (CoPc), suggesting that the valence state of Co species in Co_2/Fe-N@CHC is between 0 and +2.[13] In contrast to the reference of well-crystalline Co_3O_4, the Co_2/Fe-N@CHC does not show any fine-structure in XANES region, reflecting the formation of isolated Co species with short structural coherence length. The Fourier-transformed EXAFS (FT-EXAFS) spectrum of Co K-edge in Co_2/Fe-N@CHC shows a main peak at ~1.42 Å (**Figure 2c**), similar to that in Co_2-N@CHC (Figure S19, Supporting Information) and CoPc, which is typically assigned to the Co-N coordination at first shell.[7c, 13] Meanwhile in both Co_2/Fe-N@CHC and Co_2-N@CHC, a secondary small peak was also definitely observed at ~2.10 Å that cannot be found in CoPc, strongly demonstrating the existence of Co-Co coordination.[7b-d] The Co K-edge wavelet

transform (WT)-EXAFS was also applied to investigate the atomic configuration of Co_2/Fe-N@CHC because this spectrum can provide a sensitive measure for identifying the atomic arrangement of back scatterers in both R-space and *k*-space. The WT contour plots in Co_2/Fe-N@CHC exhibited only one intensity maximum at approximately k = 6.6 $Å^{-1}$ (**Figure 2d**), which is very similar to that in CoPc, further indicating the isolated feature of Co species rather than crystalline structure in Co_2/Fe-N@CHC. To quantitatively determine the coordination configuration (including the bond lengths and coordination numbers) in Co_2/Fe-N@CHC, non-linear EXAFS fitting analysis was performed (**Figure 2e**). According to the Co K-edge EXAFS fitting result of Co_2/Fe-N@CHC, Co species have three N neighbors at 1.84 Å and one Co neighbor at 2.41 Å in Co_2/Fe-N@CHC (Table S2, Supporting Information), indicating a Co_2-N_6 moiety (inset Figure 2e), which is in stark contrast to square planar Co-N_4 geometry of the reference CoPc. The FT-EXAFS and corresponding Fourier filtered EXAFS spectra of Co_2/Fe-N@CHC based on Co_2-N_6 and Co-N_4 models in Figure S20 (Supporting Information) confirm the presence of Co_2-N_6 dimers rather than Co-N_4 units. Moreover, the XANES simulation calculations were also performed to verify the structural models suggested by the EXAFS fitting result. As shown in Figure S21 (Supporting Information), a high level of consistency between experimental and simulated Co K-edge XANES spectra with dimeric Co_2N_6 model has been obtained.

The Fe K-edge XANES spectra of these specimens (**Figure 2f**) show that the absorption edge position of Fe in Co_2/Fe-N@CHC is very close to that of the iron phthalocyanine (FePc), indicating the divalent valence state of Fe species in Co_2/Fe-N@CHC. There are no fine features in XANES spectrum of Co_2/Fe-N@CHC, which is different from the reference spectrum of Fe_2O_3. This result strongly suggests the presence of isolated Fe species in Co_2/Fe-N@CHC without long-range order. The Fe K-edge FT EXAFS spectrum of Co_2/Fe-N@CHC demonstrates a predominant peak at ~1.50 Å (**Figure 2g**), which is very close to that in Fe-N@CHC (Figure S22, Supporting Information) and FePc, confirming the presence of atomically dispersed Fe-N_4 moieties.[6a, 14] Comparing with the Fe foil, no apparent peaks corresponding to Fe-Fe coordination shells appear at R = 2.2 and 4.4 Å for Co_2/Fe-N@CHC. The WT contour plots in Co_2/Fe-N@CHC show only one intensity maximum at k = 6.3 Å^{-1} (**Figure 2h**), which is very similar to that in FePc. Due to the absence of distant FT peaks related to Fe-Fe shell, the present Fe K-edge EXAFS spectrum of Co_2/Fe-N@CHC can be well-reproduced with structural model, in which each Fe atom is bonded with four N atoms at 1.96 Å (**Figure 2i** and Table S2, Supporting Information), like the case of Fe-N@CHC. In addition, the Fourier filtered EXAFS spectra of Co_2/Fe-N@CHC based on Fe_2-N_6 and Fe-N_4 models

(Figure S23 and Table S3, Supporting Information) and the XANES simulation calculations (Figure S21, Supporting Information) further confirm the presence of monomeric FeN_4 structure. Thus, for Co_2/Fe-N@CHC, Co species are stabilized in the Co_2-N_6 local structure whereas Fe species exist in the Fe-N_4 local structure.

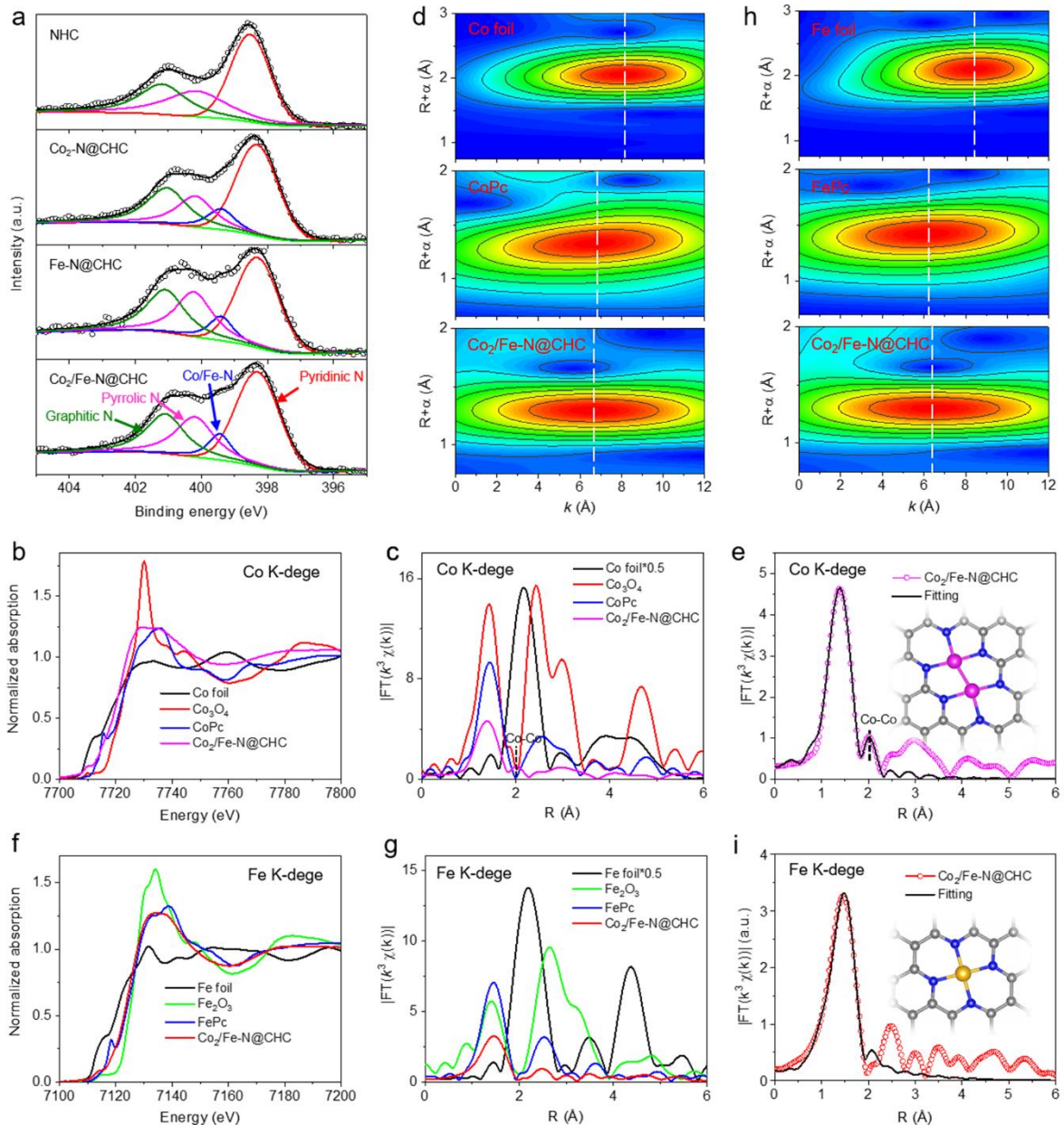

Figure 2. Chemical state and atomic local structure of Co_2/Fe-N@CHC. (a) XPS N 1s spectra of NHC, Co_2-N@CHC, Fe-N@CHC, and Co_2/Fe-N@CHC. (b) Co K-edge XANES spectra and (c) Co K-edge FT-EXAFS spectra of Co_2/Fe-N@CHC, Co foil, Co_3O_4, and CoPc. (d) Wavelet transform of the k^3-weighted EXAFS data of Co_2/Fe-N@CHC, Co foil, and CoPc. (e) Experimental and FT-EXAFS fitting curves of Co_2/Fe-N@CHC at Co K-edge, inset is the corresponding schematic model (Co: pink, N: blue, and C: black). (f) Fe K-edge XANES spectra and (g) Fe K-edge FT-EXAFS spectra of Co_2/Fe-N@CHC, Fe foil, Fe_2O_3, and FePc. (h) Wavelet transform of the k^3-weighted EXAFS data of Co_2/Fe-N@CHC, Fe foil, and FePc. (i) Experimental and FT-EXAFS fitting curves of Co_2/Fe-N@CHC at Fe K-edge, inset is the corresponding schematic model (Fe: yellow, N: blue, and C: black).

Electrochemical oxygen reduction performance

The ORR activity of the as-prepared catalysts was first characterized in O_2-saturated 0.1 M KOH solution, and the Pt/C catalyst was used for comparison. All potentials are provided versus reversible hydrogen electrode (vs. RHE). From the cyclic voltammetry (CV) curves (Figure S24, Supporting Information), Co_2/Fe-N@CHC has a well-defined cathodic peak at 0.875 V, while NHC shows a much lower one (0.716 V), implying the significant role of Co_2/Fe-N in boosting ORR kinetics. The linear sweep voltammetry (LSV) results in Figure S25 reveal that NHC exhibits a higher half-wave potential ($E_{1/2}$) than that of pyrolyzed ZIF-8, which can be attributed to its enhanced graphitized carbon shell derived from pyrolyzed PDA that facilitates electron transfer. Co_2/Fe-N@CHC presents the highest $E_{1/2}$ of 0.915 V among the as-prepared catalysts (**Figure 3a**), outperforming commercial Pt/C ($E_{1/2}$, 0.868 V), Fe-N@CHC ($E_{1/2}$, 0.894 V), Co_2-N@CHC ($E_{1/2}$, 0.880 V) and most of the state-of-the-art non-precious metal catalysts (Table S4, Supporting Information). Figure 3b shows that Co_2/Fe-N@CHC also shows a highest kinetic current density (J_k) of 9.44 mA cm^{-2} at 0.90 V, compared to Pt/C (2.91 mA cm^{-2}), Fe-N@CHC (4.68 mA cm^{-2}), and Co_2-N@CHC (3.41 mA cm^{-2}). The turnover frequency (TOF), representing the intrinsic activity of a catalyst, was estimated based on the assumption that all Co/Fe sites are available for ORR. The TOF of Co_2/Fe-N@CHC is 0.60 e^{-1} s^{-1} $sites^{-1}$ at 0.90 V, which is much higher than that of Fe-N@CHC (0.35 e^{-1} s^{-1} $sites^{-1}$) and Co_2-N@CHC (0.24 e^{-1} s^{-1} $sites^{-1}$), indicating a cooperative effect in improving electrocatalytic kinetics at the ternary-atom catalyst for ORR. Additionally, Co_2/Fe-N@CHC also delivers the highest mass activity (31.46 A g^{-1}) among the as-prepared catalysts at 0.90 V (Figure S26). The smaller Tafel slop of Co_2/Fe-N@CHC (62 mV dec^{-1}) compared with that of Pt/C (70 mV dec^{-1}), Fe-N@CHC (68 mV dec^{-1}), and Co_2-N@CHC (72 mV dec^{-1}) further confirmed its superior ORR kinetics (**Figure 3c** and Figure S27, Supporting Information).

The rotating disk electrode (RDE) measurements at various rotation rates were carried out to assess the ORR pathway of Co_2/Fe-N@CHC (**Figure 3d**). The electron transfer number, calculated from the Koutecky-Levich (K-L) curves (inset of Figure 3d), of Co_2/Fe-N@CHC is in the range of 3.97-3.99, which is larger than that of the as-prepared counterparts (Figure S28, Supporting Information), indicating a near four-electron ORR pathway. The rotating ring-disk electrode (RRDE) measurements demonstrate that the H_2O_2 yield of Co_2/Fe-N@CHC remains below 4.15% over the scanned potential range and the electron-transfer number is 3.91-3.98 (**Figure 3e**), confirming a high selectivity for four-electron reduction of O_2 to H_2O. No major decay in $E_{1/2}$ (with only 7 mV negative shift) is observed after 10,000 continuous potential

cycles (**Figure 3f**). The outstanding stability is also supported by the chronoamperometry measurement (**Figure 3g**), where Co_2/Fe-N@CHC retains 91.1% of initial current over 100 hours continuous operation in an O_2-saturated electrolyte. However, the current retention is only a 66.1% for commercial Pt/C over 50 hours test under the same alkaline condition. Furthermore, the HAADF-STEM and XRD analysis of the used Co_2/Fe-N@CHC after stability test show that the Co_2/Fe dual atoms still remain well dispersed on the carbon supports without observable aggregation (Figure S29, Supporting Information), indicating structural robustness and stability of Co_2/Fe-N@CHC. The chronoamperometric responses for ORR at 0.7 V upon the immediate addition of methanol were also measured. As shown in **Figure 3h**, about 300 s after the addition of methanol into the electrolyte, the relative current of Pt/C drops sharply, whereas the current changes only slightly for Co_2/Fe-N@CHC, suggesting the superior tolerance to methanol crossover effects.

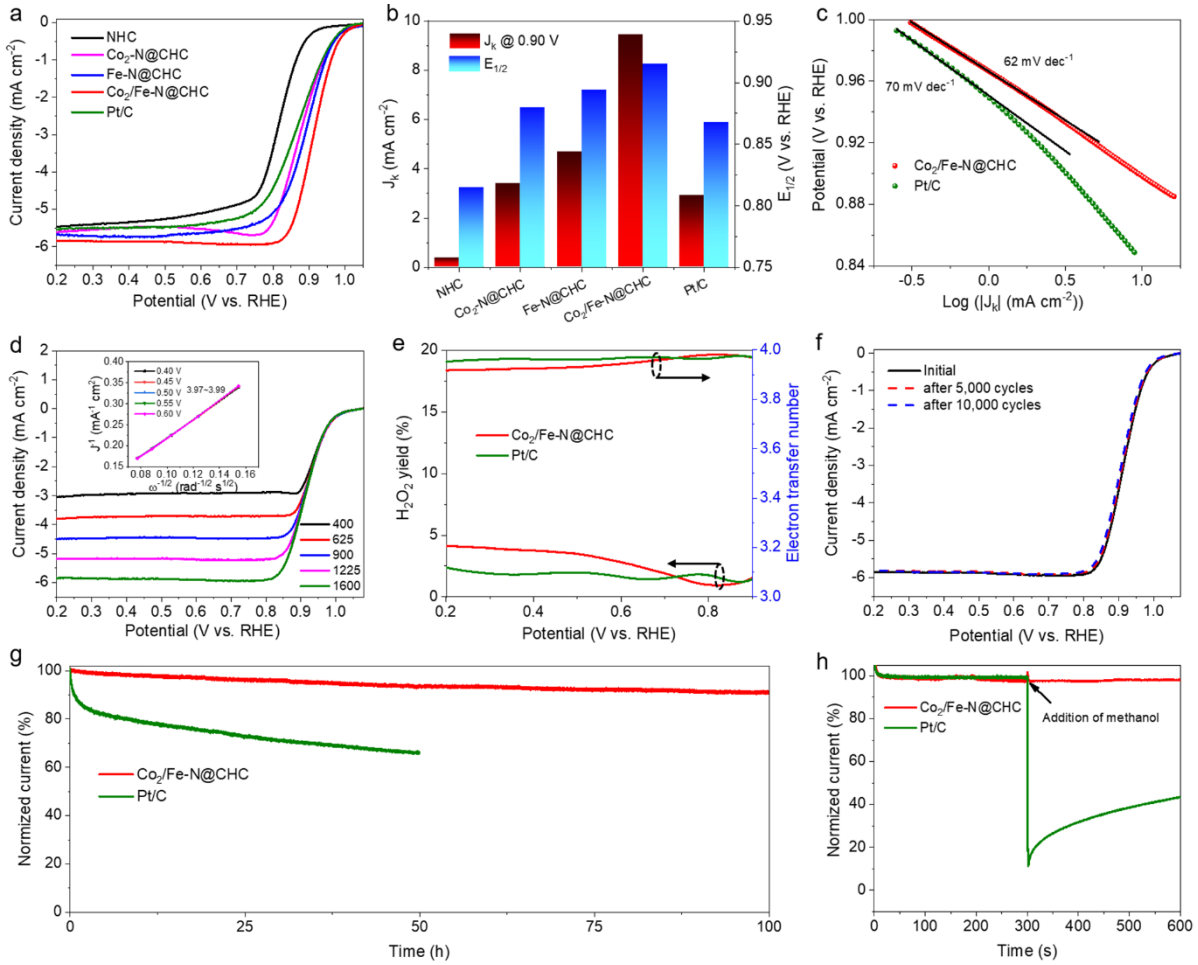

Figure 3. Electrocatalytic oxygen reduction reaction (ORR) activity and durability evaluations. (a) Linear sweep voltammetry (LSV) curves of NHC, Co_2-N@CHC, Fe-N@CHC, Co_2/Fe-N@CHC, and Pt/C in O_2-staurated 0.1 M KOH solution at 1600 rpm. (b) Kinetic current density (J_k) at 0.90 V and half-wave potential ($E_{1/2}$) for these catalysts. (c) Tafel slopes for Co_2/Fe-N@CHC and Pt/C. (d) LSV curves of Co_2/Fe-N@CHC at different rotating rates (inset: the corresponding K-L plots and electron

transfer number). (e) H_2O_2 yield and electron transfer number of Co_2/Fe-N@CHC and Pt/C vs. potential. (f) LSV curves of Co_2/Fe-N@CHC before and after 10,000 potential cycles. (g) Normalized chronoamperometry curves of Co_2/Fe-N@CHC and Pt/C at constant potentials of 0.7 V. (h) Methanol tolerance tests.

The ORR performance of Co_2/Fe-N@CHC in a more challenging acidic condition (0.1 M $HClO_4$) was also investigated (data are presented in **Figure S30**, Supporting Information). The ORR activity with a $E_{1/2}$ of 0.812 V for the Co_2/Fe-N@CHC is much higher than those of Co_2-N_6@CHC (0.770 V) and Fe-N_4@CHC (0.787 V), and even comparable to that of commercial Pt/C (0.835 V). The Co_2/Fe-N@CHC also exhibits a J_k of 8.36 mA cm^{-2} at 0.80 V and a low Tafel slope of 73 mV dec^{-1}, approaching that of commercial Pt/C (71 mV dec^{-1}), suggesting a favorable ORR kinetic. The RRDE measurements give a quite low H_2O_2 yield (below 1.5%) for Co_2/Fe-N@CHC with a high electron transfer number ranging from 3.97-3.99, which is consistent with the result from K-L plots. The methanol tolerance in acidic electrolyte is also quite good as the current does not change obviously when methanol is added (Figure S31, Supporting Information). Moreover, the accelerated durability test demonstrates stability of Co_2/Fe-N@CHC with only 9 mV decay on $E_{1/2}$ after 5000 cycles, which is even lower than that of Pt/C (21 mV) under the same condition (Figure S30, Supporting Information). From these results, it can be inferred that Co_2/Fe-N@CHC is a promising candidate for ORR in both alkaline and acidic electrolytes.

Catalytic mechanism and theoretical calculations

Density functional theory (DFT) calculations were performed to study the critical role of the ternary-atom sites (Co_2/Fe-N_{10}) in boosting ORR activity. Four representative models for Co_2/Fe-N_{10} system with different possible arrangements and distances between Co_2-N_6 and Fe-N_4 sites have been constructed and optimized in terms of energy and force (Figures S32 and S33, Supporting Information), from which the energetically most favorable configuration is identified (**Figure 4a**). For comparison, two other models, dual-atom Co_2-N_6 and single-atom Fe-N_4 structures, were also constructed. Based on the experimental results, the associated mechanism with four-electrons pathway was adopted for DFT calculations (computational details are presented in Supporting Information). The Gibbs free energy diagrams for ORR with the four configurations, viz., Fe-N_4 site in Co_2/Fe-N_{10}, Fe-N_4 structure, Co_2-N_6 site in Co_2/Fe-N_{10}, and Co_2-N_6 structure are calculated (see **Figure 4b** and Figure S34, Supporting Information). Fe-N_4 site in Co_2/Fe-N_{10} and Fe-N_4 structure possess a consistent downhill energy pathway at U = 0 V, indicating a spontaneous exothermal process. Upon increasing the potential

to 1.23 V, the highest uphill free energy from the fourth electron transfer step (*OH + e^- → OH^-) determines the rate-determining step (RDS) for both Fe-N_4 site in Co_2/Fe-N_{10} and Fe-N_4 structure. The Fe-N_4 site in Co_2/Fe-N_{10} has a lower overpotential (0.569 V) than that of single-atom Fe-N_4 structure (0.665 V), suggesting a more efficient ORR activity for Co_2/Fe-N_{10} due to the Co_2N_6 site. The in-situ Raman spectroscopic spectra give the direct evidence for the generation of O-containing intermediates on the surface of Co_2/Fe-N_{10} sites in Co_2/Fe-N@CHC (**Figure 4c**). The broad Raman band around 1150 cm^{-1}, due to the O-O stretching vibration of O_2^-, appeared when the potential was decreased to 0.8 V (vs. RHE).[15] With further decrease in the potential, this peak becomes stronger, indicating more O_2^--Co_2/Fe-N_{10} intermediates are formed. The optimized configurations of intermediates (*OOH, *O, and *OH) on Fe-N_4 site in Co_2/Fe-N_{10} are shown in Figure S35 (Supporting Information). In the case of Co_2-N_6 structure, the energy barrier of the RDS (*O + H_2O + e^- → *OH + OH^-) is calculated to be 1.560 V (Figure S34, Supporting Information), implying the over-strong adsorption of *O intermediates on Co_2-N_6 moiety. This limits the whole ORR reaction on Co_2-N_6 structure. In addition, the energy difference between *O and *OH intermediates on the Co_2-N_6 site in Co_2/Fe-N_{10} system has a reduction by 0.624 V compared to that for dual-atom Co_2-N_6 structure, and the energy barrier of RDS (*OH + e^- → OH^-) is calculated to be 1.224 V (Figure S34, Supporting Information), which is still much higher than that of Fe-N_4 site in Co_2/Fe-N_{10} due to its strong absorption of *OH intermediates. According to above results and discussion, the lower energy barriers of RDS for Fe-N_4 site in Co_2/Fe-N_{10} system compared to the counterparties (sing-atom Fe-N_4 and dual-atom Co_2-N_6 structures) demonstrate the existence of synergistic effect between Fe-N_4 and Co_2-N_6 in Co_2/Fe-N_{10} towards enhanced ORR catalytic activity, which is also consistent with the experimental results.

To further investigate the underlying origin of the superior ORR activity for Co_2/Fe-N@CHC, the electronic structure features of Fe-center and Co-center moieties were also studied. **Figure 4d** shows the calculated difference charge densities for adsorption O on Fe-N_4 and Co_2-N_6 sites in Co_2/Fe-N_{10}. The charge mainly transfers from active metal site to O atom and surrounding N atoms in both cases. It should be noted that the amount of the transferred charge on Co_2-N_6 site is larger than that on Fe-N_4 site. We performed the Bader charge analysis to quantitatively assess this transfer (Table S5, Supporting Information).[16] The Bader charge state of Fe (Co_2) is 1.31|e| (1.93|e|), which is mainly transferred to nearby in-plane N atoms with an averaged Bader charge state of -1.14 |e| (-1.16 |e|) and O atom with a value of -0.64|e| (-0.71|e|). The more net charge gains of adsorbed O on Co_2-N_6 site indicate a relatively stronger binding energy of O adsorption when compared to that on Fe-N_4 site. These results rationalize

the large difference of the overpotentials on Fe-N_4 and Co_2-N_6 sites in Co_2/Fe-N_{10} system. The projected density of states (PDOS) of Fe atoms in Co_2/Fe-N_{10} and Fe-N_4 systems were also presented to further probe the crucial role of Co_2-N_6 site in assisting Fe-N_4 site for enhancing the ORR performance. As shown in **Figure 4e**, the obvious shift of Fe-d orbitals towards lower energy level can be observed for Co_2/Fe-N_{10} compared to Fe-N_4. This is in agreement with the corresponding Fe d-band center being -1.296 and -0.736 eV for Co_2/Fe-N_{10} and Fe-N_4, respectively (Table S6, Supporting Information). A more negative value of d-band center would produce an increased anti-bonding orbitals filling, which decreases the interaction between the active sites and the adsorbates. Therefore, the existence of Co_2-N_6 could finally enhance the ORR activities on Fe-N_4 site in Co_2/Fe-N_{10} system. In detail, the negative shift of PDOS in Co_2/Fe-N_{10} leads to increased filling degree of the anti-bonding d_{z2}, d_{xz}, and d_{yz} orbitals of Fe atom.[12b] These enhanced filling of anti-bonding orbitals of Fe in Co_2/Fe-N_{10} would yield weakened σ and π bonds with adsorbed *OH on Fe-center, thus facilitating ORR process. These results provide a physical insight into the synergistic effect of Fe-N_4 and Co_2-N_6 sites in Co_2/Fe-N_{10}, fully in consistence with the observed enhanced activity of the Co_2/Fe-N@CHC catalyst.

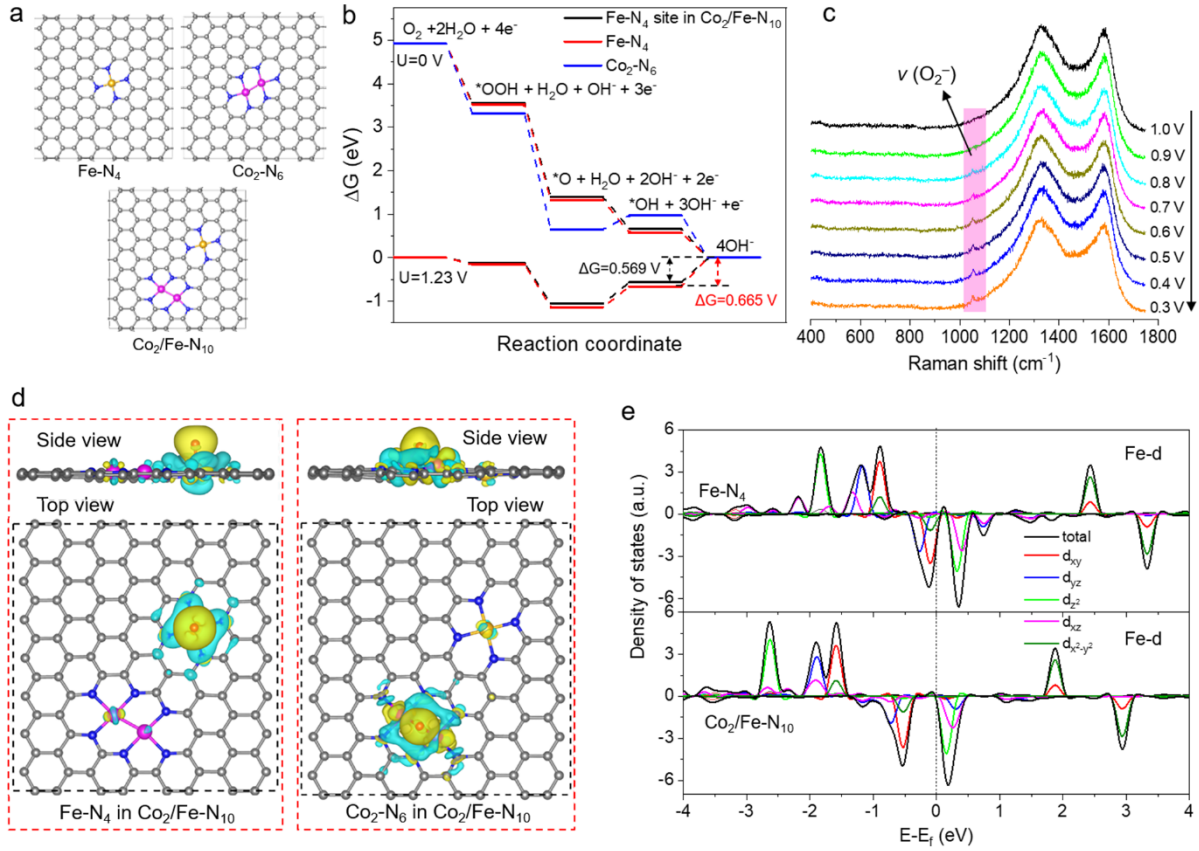

Figure 4. Density functional theory calculations of ORR on Co_2/Fe-N_{10}, Fe-N_4, and Co_2-N_6. (a) Illustration of representative atomic configurations of Fe-N_4, Co_2-N_6, and Co_2/Fe-N_{10}. (b) ORR free energy diagrams for Fe-N_4 site in Co_2/Fe-N_{10} (black line), Fe-N_4 (red line), and Co_2-N_6 (blue line) at U = 0 and 1.23 V. (c) In-situ Raman spectra of Co_2/Fe-N@CHC recorded at various potentials in O_2-

saturated 0.1 M KOH electrolyte. (d) The difference charge density plots of O adsorption on Fe-N_4 (left) and Co_2-N_6 (right) sites in Co_2/Fe-N_{10}, respectively; the charge accumulation and depletion regions are represented in yellow and blue, respectively. (e) The projected density of states (PDOS) of Fe-d orbitals in Fe-N_4 (above) and Co_2/Fe-N_{10} (below).

Zinc-air battery performance

To evaluate the effectiveness of Co_2/Fe-N@CHC in renewable energy devices, we incorporated Co_2/Fe-N@CHC in a practical cathode of the Zn-air battery (ZAB) and tested its performance in atmospheric environment (**Figure 5a**). For comparison, the ZAB using commercial Pt/C as air cathode catalyst was also assembled. As shown in **Figure 5b**, Co_2/Fe-N@CHC-based ZAB exhibits an open-circuit voltage (OCV) of 1.499 V, higher than that of the Pt/C-based counterpart (1.481 V) (Figure S36, Supporting Information). Moreover, a maximum power density of 232.4 mW cm^{-2} is achieved from the ZAB based on Co_2/Fe-N@CHC (**Figure 5c**), outperforming the Pt/C-based ZAB (189.1 mW cm^{-2}) as well as ZABs made from other recent-reported catalysts (Table S7, Supporting Information). The discharge current density ranging from 5 to 50 mA cm^{-2} was periodically changed every 2 hours, during which the Co_2/Fe-N@CHC-based ZAB show staircase like voltage response over 30 hours (**Figure 5d** top). At a fixed current density of 10 mA cm^{-2}, no significant change of discharge voltage is observed for 200 hr run (Figure 5d bottom). At the discharge current density of 10 mA cm^{-2}, the specific capacity of Co_2/Fe-N@CHC-based ZAB was estimated to be 786.1 mAh g^{-1} (Figure S37, Supporting Information), superior to the Pt/C-based ZAB (740.2 mAh g^{-1}). In addition, the cycling performance of Co_2/Fe-N@CHC+RuO_2 (with a mass ratio of 1/1)-based ZAB was investigated by galvanostatic charge-discharge cycles with a duration of 40 min per cycle (**Figure 5e**). In the initial cycle, this ZAB yields a discharge voltage of 1.259 V and a charge voltage of 2.003 V, corresponding to a voltage efficiency of 62.85%. Negligible voltage fading for both charge and discharge processes can be observed over 240 h (360 cycles) for Co_2/Fe-N@CHC+RuO_2-based ZAB, while the discharge voltage of the Pt/C+RuO_2-based device dropped evidently within 100 hours under the same test condition (Figure S38, Supporting Information), confirming the outstanding stability of Co_2/Fe-N@CHC in practical ZABs.

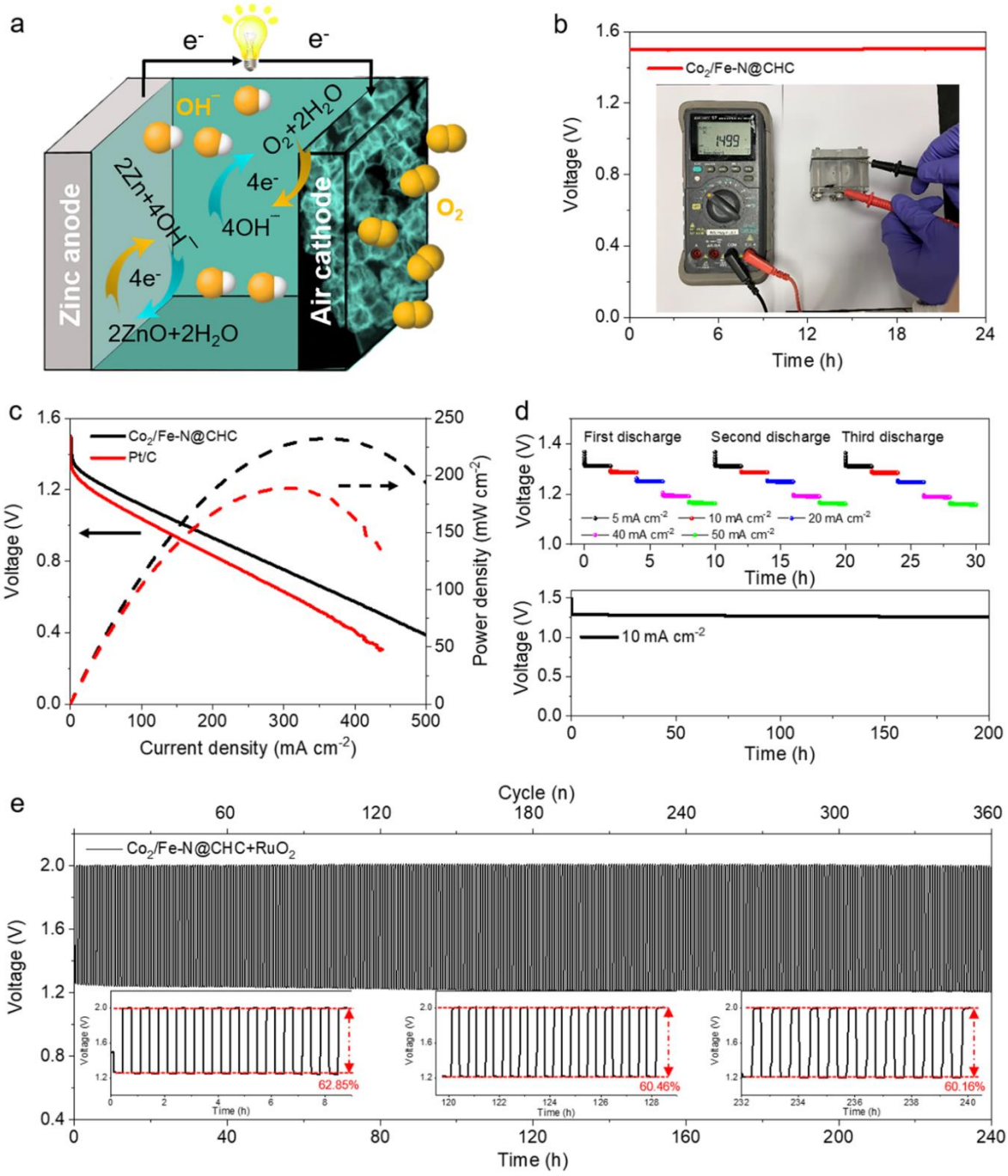

Figure 5. Zn-air battery (ZAB) performance. (a) Schematic configuration of the homemade ZAB. (b) Open circuit voltage of the ZAB based on Co_2/Fe-N@CHC. (c) Discharge polarization curves and corresponding power densities of ZABs based on Co_2/Fe-N@CHC and Pt/C. (d) Cycle discharge curves of Co_2/Fe-N@CHC-based ZAB at periodically changed current densities of 5, 10, 20, 40, and 50 mA cm^{-2} (top), and longtime discharge curve at 10 mA cm^{-2} (bottom). (e) Galvanostatic change/discharge cycling performance of ZAB based on Co_2/Fe-N@CHC+RuO_2 at a current density of 5 mA cm^{-2}. Insets are the corresponding voltage efficiency graphs during the cycling test.

In conclusion, ternary-atom Co_2/Fe sites coordinated with nitrogen atoms (Co_2/Fe-N_{10}) anchored on CNTs-grafted hollow carbon nanocages have been realized via facile polydopamine and pyrolytic strategies. The co-existence of Co_2-N_6 and Fe-N_4 sites has been

identified, which renders strongly enhanced catalytic activity for ORR in both alkaline and acid conditions compared to single-atom Fe-N_4 and dual-atom Co_2-N_6 counterparts. DFT calculations reveal that the existence of Co_2-N_6 site in Co_2/Fe-N@CHC effectively increases the charge filling degree of anti-bonding orbitals of Fe center of the Fe-N_4 site, which consequently lowers the energy barrier for the rate determining step (*OH desorption), and thus enhances the intrinsic ORR catalytic activity of the Co_2/Fe-N_{10} system. When used as the catalyst for cathodic ORR in zinc-air batteries, our uniquely designed Co_2/Fe-N@CHC electrode exhibits a higher power density of 232.4 mW cm^{-2} and better cycling stability than that of Pt-based one. This work paves a way for rationally engineering the geometric and electronic structures of metal active centers to boost ORR activity for energy storage and conversion devices.

Supporting Information

Supporting Information is available from the Wiley Online Library or from the author.

Acknowledgements

H.J. F. thanks the financial support from Agency for Science, Technology, and Research (A*STAR), Singapore by AME Individual Research Grants (A1983c0026). S.-J. H thanks the financial support from the National Research Foundation of Korea (NRF) grant funded by the Korea government (MSIP) (No. NRF-2020R1A2C3008671). The experiments at PAL were supported in part by MOST and POSTECH.

Received: ((will be filled in by the editorial staff))
Revised: ((will be filled in by the editorial staff))
Published online: ((will be filled in by the editorial staff))

Conflict of Interest

The authors declare no conflict of interest.

References

[1] a) W. Sun, B. Zhang, M. Zhang, V. Küpers, X. Ji, C. Theile, P. Bieker, K. Xu, C. Wang, M. Winter, *Science* **2021**, 371, 46; b) T. Sun, S. Mitchell, J. Li, P. Lyu, X. Wu, J. Perez-Ramirez, J. Lu, *Adv. Mater.* **2021**, 33, e2003075; c) J. Li, M. Chen, D. A. Cullen, S. Hwang, M. Wang, B. Li, K. Liu, S. Karakalos, M. Lucero, H. Zhang, C. Lei, H. Xu, G. E. Sterbinsky, Z. Feng, D. Su, K. L. More, G. Wang, Z. Wang, G. Wu, *Nat. Catal.* **2018**, 1, 935; d) J. Chen, H. Li, C. Fan, Q. Meng, Y. Tang, X. Qiu, G. Fu, T. Ma, *Adv. Mater.* **2020**, 32, e2003134; e) Y. Wang, F. Chu, J. Zeng, Q. Wang, T. Naren, Y. Li, Y. Cheng, Y. Lei, F. Wu, *ACS Nano* **2021**, 15, 210.

[2] M. Luo, Z. Zhao, Y. Zhang, Y. Sun, Y. Xing, F. Lv, Y. Yang, X. Zhang, S. Hwang, Y. Qin, J. Y. Ma, F. Lin, D. Su, G. Lu, S. Guo, *Nature* **2019**, 574, 81.

[3] a) L. Chong, J. Wen, J. Kubal, F. G. Sen, J. Zou, J. Greeley, M. Chan, H. Barkholtz, W. Ding, D.-J. Liu, *Science* **2018**, 362, 1276; b) G. Yang, J. Zhu, P. Yuan, Y. Hu, G. Qu, B. A. Lu, X. Xue, H. Yin, W. Cheng, J. Cheng, W. Xu, J. Li, J. Hu, S. Mu, J. N. Zhang, *Nat. Commun.* **2021**, 12, 1734; c) Q. Yang, Y. Jia, F. Wei, L. Zhuang, D. Yang, J. Liu, X. Wang, S. Lin, P. Yuan, X. Yao, *Angew. Chem. Int. Ed.* **2020**, 59, 6122; d) Y. Chen, Z. Li, Y. Zhu, D. Sun, X. Liu, L. Xu, Y. Tang, *Adv. Mater.* **2019**, 31, e1806312; e) Y. Chen, S. Ji, S. Zhao, W. Chen, J. Dong, W. C. Cheong, R. Shen, X. Wen, L. Zheng, A. I. Rykov, S. Cai, H. Tang, Z. Zhuang, C. Chen, Q. Peng, D. Wang, Y. Li, *Nat. Commun.* **2018**, 9, 5422; f) X. Tian, Y.-Q. Su, L. Wang, H. Wang, D. Dang, B. Chi, H. Liu, E. J.M. Hensen, X. W. Lou, B. Y. Xia, *Science* **2019**, 3666, 850.

[4] C. X. Zhao, B. Q. Li, J. N. Liu, Q. Zhang, *Angew. Chem. Int. Ed.* **2021**, 60, 4448.

[5] a) L. Li, X. Chang, X. Lin, Z. J. Zhao, J. Gong, *Chem. Soc. Rev.* **2020**, 49, 8156; b) S. Ding, M. J. Hülsey, J. Pérez-Ramírez, N. Yan, *Joule* **2019**, 3, 2897; c) C. Wan, X. Duan, Y. Huang, *Adv. Energy Mater.* **2020**, 10, 1903815; d) C. Lu, R. Fang, X. Chen, *Adv. Mater.* **2020**, 32, e1906548; e) P. Yin, B. You, *Mater. Today Energy* **2021**, 19, 100586.

[6] a) R. Jiang, L. Li, T. Sheng, G. Hu, Y. Chen, L. Wang, *J. Am. Chem. Soc.* **2018**, 140, 11594; b) Y. Qu, Z. Li, W. Chen, Y. Lin, T. Yuan, Z. Yang, C. Zhao, J. Wang, C. Zhao, X. Wang, F. Zhou, Z. Zhuang, Y. Wu, Y. Li, *Nat. Catal.* **2018**, 1, 781; c) Y. Mun, S. Lee, K. Kim, S. Kim, S. Lee, J. W. Han, J. Lee, *J. Am. Chem. Soc.* **2019**, 141, 6254; d) X. Wang, Y. Jia, X. Mao, D. Liu, W. He, J. Li, J. Liu, X. Yan, J. Chen, L. Song, A. Du, X. Yao, *Adv. Mater.* **2020**, 32, e2000966; e) Y. Zhou, X. Tao, G. Chen, R. Lu, D. Wang, M. X. Chen, E. Jin, J. Yang, H. W. Liang, Y. Zhao, X. Feng, A. Narita, K. Mullen, *Nat. Commun.* **2020**, 11, 5892; f) L. Jiao, R. Zhang, G. Wan, W. Yang, X. Wan, H. Zhou, J. Shui, S. H. Yu, H. L. Jiang, *Nat. Commun.* **2020**, 11, 2831; g) H. Shang, Z. Jiang, D. Zhou, J. Pei, Y. Wang, J. Dong, X. Zheng, J. Zhang, W. Chen, *Chem. Sci.* **2020**, 11, 5994; h) Z. Jiang, W. Sun, H. Shang, W. Chen, T. Sun, H. Li, J. Dong, J. Zhou, Z. Li, Y. Wang, R. Cao, R. Sarangi, Z. Yang, D. Wang, J. Zhang, Y. Li, *Energy Environ. Sci.* **2019**, 12, 3508.

[7] a) Y. S. Wei, L. Sun, M. Wang, J. Hong, L. Zou, H. Liu, Y. Wang, M. Zhang, Z. Liu, Y. Li, S. Horike, K. Suenaga, Q. Xu, *Angew. Chem. Int. Ed.* **2020**, 59, 16013; b) X. Han, X. Ling, D. Yu, D. Xie, L. Li, S. Peng, C. Zhong, N. Zhao, Y. Deng, W. Hu, *Adv. Mater.* **2019**, 31, e1905622; c) Z. Lu, B. Wang, Y. Hu, W. Liu, Y. Zhao, R. Yang, Z. Li, J. Luo, B. Chi, Z. Jiang, M. Li, S. Mu, S. Liao, J. Zhang, X. Sun, *Angew. Chem. Int. Ed.* **2019**, 58, 2622; d) M. Xiao, Y. Chen, J. Zhu, H. Zhang, X. Zhao, L. Gao, X. Wang, J. Zhao, J. Ge, Z. Jiang, S. Chen, C. Liu, W. Xing, *J. Am. Chem. Soc.* **2019**, 141, 17763; e) M. Tong, F. Sun, Y. Xie, Y. Wang, Y. Yang, C. Tian, L. Wang, H. Fu, *Angew. Chem. Int. Ed.* **2021**, 60, 2; f) Z. Zhu, H. Yin, Y. Wang, C. H. Chuang, L. Xing, M. Dong, Y. R. Lu, G. Casillas-Garcia, Y. Zheng, S. Chen, Y. Dou, P. Liu, Q. Cheng, H. Zhao, *Adv. Mater.* **2020**, 32, e2004670.

[8] a) X. Wei, D. Zheng, M. Zhao, H. Chen, X. Fan, B. Gao, L. Gu, Y. Guo, J. Qin, J. Wei, Y. Zhao, G. Zhang, *Angew. Chem. Int. Ed.* **2020**, 59, 14639; b) Z. Zhang, X. Zhao, S. Xi, L. Zhang, Z. Chen, Z. Zeng, M. Huang, H. Yang, B. Liu, S. J. Pennycook, P. Chen, *Adv. Energy Mater.* **2020**, 10, 2002896; c) H. Shang, X. Zhou, J. Dong, A. Li, X. Zhao, Q. Liu, Y. Lin, J. Pei, Z. Li, Z. Jiang, D. Zhou, L. Zheng, Y. Wang, J. Zhou, Z. Yang, R. Cao, R. Sarangi, T. Sun, X. Yang, X. Zheng, W. Yan, Z. Zhuang, J. Li, W. Chen, D. Wang, J. Zhang, Y. Li, *Nat. Commun.* **2020**, 11, 3049; d) L. Gong, H. Zhang, Y. Wang, E. Luo, K. Li, L. Gao, Y. Wang, Z. Wu, Z. Jin, J. Ge, Z. Jiang, C. Liu, W. Xing, *Angew. Chem. Int. Ed.* **2020**, 59, 13923; e) X. Hai, X. Zhao, N. Guo, C. Yao, C. Chen, W. Liu, Y. Du, H. Yan, J. Li, Z. Chen, X. Li, Z. Li, H. Xu, P. Lyu, J. Zhang, M. Lin, C. Su, S. J.

Pennycook, C. Zhang, S. Xi, J. Lu, *ACS Catalysis* **2020**, 10, 5862; f) T. Sun, Y. Li, T. Cui, L. Xu, Y. G. Wang, W. Chen, P. Zhang, T. Zheng, X. Fu, S. Zhang, Z. Zhang, D. Wang, Y. Li, *Nano Lett.* **2020**, 20, 6206; g) Y. Chen, R. Gao, S. Ji, H. Li, K. Tang, P. Jiang, H. Hu, Z. Zhang, H. Hao, Q. Qu, X. Liang, W. Chen, J. Dong, D. Wang, Y. Li, *Angew. Chem. Int. Ed.* **2021**, 60, 3212.

[9] J. Zhang, H. Yang, B. Liu, *Adv. Energy Mater.* **2021**, 11, 2002473.

[10] a) J. Wang, W. Liu, G. Luo, Z. Li, C. Zhao, H. Zhang, M. Zhu, Q. Xu, X. Wang, C. Zhao, Y. Qu, Z. Yang, T. Yao, Y. Li, Y. Lin, Y. Wu, Y. Li, *Energy Environ Sci* **2018**, 11, 3375; b) H. Sun, M. Wang, S. Zhang, S. Liu, X. Shen, T. Qian, X. Niu, J. Xiong, C. Yan, *Adv. Funct. Mater.* **2021**, 31, 2006533.

[11] Y. Liang, J. Wei, Y. X. Hu, X. F. Chen, J. Zhang, X. Y. Zhang, S. P. Jiang, S. W. Tao, H. T. Wang, *Nanoscale* **2017**, 9, 5323.

[12] a) L. Zhao, Y. Zhang, L. B. Huang, X. Z. Liu, Q. H. Zhang, C. He, Z. Y. Wu, L. J. Zhang, J. Wu, W. Yang, L. Gu, J. S. Hu, L. J. Wan, *Nat. Commun.* **2019**, 10, 1278; b) D. Xia, X. Yang, L. Xie, Y. Wei, W. Jiang, M. Dou, X. Li, J. Li, L. Gan, F. Kang, *Adv. Funct. Mater.* **2019**, 29, 1906174; c) X. Xie, L. Peng, H. Yang, G. I. N. Waterhouse, L. Shang, T. Zhang, *Adv. Mater.* **2021**, e2101038; d) H. Tian, H. Tian, S. Wang, S. Chen, F. Zhang, L. Song, H. Liu, J. Liu, G. Wang, *Nat. Commun.* **2020**, 11, 5025.

[13] Y. Ha, B. Fei, X. Yan, H. Xu, Z. Chen, L. Shi, M. Fu, W. Xu, R. Wu, *Adv. Energy Mater.* **2020**, 10, 2002592.

[14] C. C. Hou, L. Zou, L. Sun, K. Zhang, Z. Liu, Y. Li, C. Li, R. Zou, J. Yu, Q. Xu, *Angew. Chem. Int. Ed.* **2020**, 59, 7384.

[15] J.-C. Dong, X.-G. Zhang, V. Briega-Martos, X. Jin, J. Yang, S. Chen, Z.-L. Yang, D.-Y. Wu, J. M. Feliu, C. T. Williams, Z.-Q. Tian, J.-F. Li, *Nat. Energy* **2018**, 4, 60.

[16] G. Henkelman, A. Arnaldsson, H. Jónsson, *Comput. Mater. Sci.* **2006**, 36, 354.

WILEY-VCH

Supporting Information

Atomically dispersed Co_2-N_6 and Fe-N_4 co-structures boost oxygen reduction reaction in both alkaline and acidic media

Zhe Wang, Xiaoyan Jin, Chao Zhu, Yipu Liu, Hua Tan, Ruiqi Ku, Yongqi Zhang, Liujiang Zhou, Zheng Liu, Seong-Ju Hwang,* Hong Jin Fan**

Dr. Z. Wang, Dr. Y. Liu, Dr. H. Tan, Prof. H. J. Fan
School of Physical and Mathematical Sciences, Nanyang Technological University, 21 Nanyang Link, 637371, Singapore
E-mail: fanhj@ntu.edu.sg

Dr. Z. Wang, Dr. C. Zhu, Prof. Z. Liu
School of Materials Science and Engineering, Nanyang Technological University, 50 Nanyang Avenue, 639798, Singapore

Dr. X. Jin, Prof. S.-J. Hwang
Department of Materials Science and Engineering, Yonsei University, Seoul 03722, Republic of Korea
E-mail: hwangsju@yonsei.ac.kr

R. Ku, Prof. Y. Zhang, Prof. L. Zhou
Institute of Fundamental and Frontier Sciences, University of Electronic Science and Technology of China, Chengdu 610054, China.
E-mail: ljzhou86@uestc.edu.cn

Prof. Y. Zhang, Prof. L. Zhou
Yangtze Delta Region Institute (Huzhou), University of Electronic Science and Technology of China, Huzhou 313001, China.

Experimental Section

Materials synthesis

Synthesis of CoFe-PDA@ZIF-8. In a typical synthesis of ZIF-8, 10 g of 2-methylimidazole was dissolved in 100 mL of methanol, which was subsequently added into 100 mL of methanol containing 4.7 g of $Zn(NO_3)_2 \cdot 6H_2O$ with stirring for 24 h at room temperature. The obtained product was then collected by centrifugation and washed with methanol for several times and dried at 70 °C in vacuum oven overnight. 0.2 g of as-prepared ZIF-8 and 0.12 g (1 mmol) of tris(hydroxymethyl) aminomethane were dispersed in 100 mL of a mixture (ethanol/ DI water, 1/1) by sonication and stirring to form solution A. 28.4 mg (0.15 mmol) of dopamine hydrochloride, 43.6mg (0.15 mmol) of $Co(NO_3)_2 \cdot 6H_2O$, and 30.3 mg (0.075 mmol) of $Fe(NO_3)_3 \cdot 9H_2O$ were dissolved in 100 mL of DI water to form solution B. Then solution B was added into solution A. After magnetic stirring for 4 h at room temperature, a gray solid product was collected via centrifugation and washed with DI water and ethanol for several times, and finally dried at 70 °C in vacuum oven overnight. The as-prepared products were denoted as CoFe-PDA@ZIF-8. In comparison, Co-PDA@ZIF-8, Fe-PDA@ZIF-8, and PDA@ ZIF-8 were also prepared via the similar procedure except only adding 0.225 mmol of $Co(NO_3)_2 \cdot 6H_2O$, 0.225 mmol of $Fe(NO_3)_2 \cdot 9H_2O$, and without adding cobalt and iron salts in the corresponding precursors, respectively.

Synthesis of Co_2/Fe-N@CHC. The as-prepared powers of CoFe-PDA@ZIF-8 and melamine with the ratio of 1/1 were transferred to a tube furnace to be heated under argon (Ar) environment at the following procedure: firstly heated at rate of 2 °C min^{-1} from room temperature to 550 °C, and maintained for 1 h, then heated at rate of 5 °C min^{-1} from 550 °C to 920 °C, and maintained for 2h. The obtained black powders were then immersed in 3 M H_2SO_4 solution at 80 °C for 12 h, after washing with DI water for several times and drying at 70 °C in vacuum oven overnight, the Co_2/Fe-N@CHC was obtained. Co_2-N@CHC and Fe-N@CHC were prepared in the same way with that of Co_2/Fe-N@CHC by using Co-PDA@ZIF-8, and Fe-PDA@ZIF-8 as precursors, respectively. NHC and pyrolyzed ZIF-8 were also prepared by annealing PDA@ZIF-8 and ZIF-8, respectively, under the same condition.

Characterizations

The composition and crystal structure of the synthesized materials were characterized by an X-ray powder diffractometer (XRD, Bruker D8 Advance XRD, equipped with Cu Kα radiation, λ=1.5406 Å). The morphologies of the as-prepared samples were studied by field-emission scanning electron microscopy (FESEM, JEOL, JSM-7600F), transmission electron microscopy (TEM, JEOL, JEM-2100F), and high-angle annular dark-field scanning transmission electron microscope (HAADF-STEM, JEM-ARM300F), equipped with a probe corrector. The Brunauer-Emmett-Teller (BET) specific surface area and porous structure were evaluated at 77 K on a Micromeritics ASAP 2020 system. X-ray photoelectron spectroscopy (XPS) measurements were carried out on a Kratos Axis Supra electron spectrometer to analyze surface chemistry. The elemental compositions were measured by inductively coupled plasma atomic emission spectroscopy (ICP-OES). Raman spectroscopy was performed on a Renishaw Raman microscope with the laser wavelength of 532 nm. The local structures of the present materials were investigated by measuring the Co K-edge and Fe K-edge X-ray absorption near-edge structure (XANES) and the extended X-ray absorption fine structure (EXAFS) data at beam line 10C in the Pohang Accelerator Laboratory (PAL, Pohang, Korea). The energy calibration for the present XANES/EXAFS spectra was done by simultaneously measuring the reference spectrum of Co and Fe metal foil. All the measured XANES/EXAFS spectra were collected at room temperature in a transmission mode using gas-ionization detectors.

Electrochemical measurements

All electrochemical measurements were performed on an electrochemical analysis workstation (760E, CH Instrument) using a standard three-electrode system, which comprises of a graphene rod counter electrode, an Ag/AgCl (3M KCl solution) reference electrode and a working electrode. The working electrode was prepared by dropping the catalyst ink onto a glass-carbon (GC), which is a rotating disk electrode (RDE, 5 mm in diameter) or a rotating ring-disk electrode (RRDE, 5.5 mm in diameter). The catalyst ink was prepared by dispersing 5 mg of each catalyst in 1mL of mixed solution containing 0.98 mL of ethanol/water (1:1, v/v) and 20 μL of 5 wt% Nafion solution, followed by ultra-sonication for 30 min to form a homogeneous black suspension solution. Then the as-obtained catalyst ink was drop-casted onto the surface of GC electrode followed by drying in air. The catalyst loading amount for both as-prepared catalysts and commercial Pt/C (20 wt%) was 0.3 mg cm^{-2}.

The ORR performance of the catalysts was measured in O_2-saturated 0.1 M KOH solution. The cyclic voltammetry (CV) curves were obtained at a scan rate of 50 mV s^{-1}. Linear sweep voltammetry (LSV) was performed using RDE/RRDE at a scan rate of 5 mV s^{-1} with various

rotation speeds (400, 625, 900, 1225 and 1,600 rpm). All measured potentials are provided versus the standard reversible hydrogen electrode (RHE). The onset potential was defined as the potential required for generating a current density of -0.1 mA cm^{-2} in LSV curves. The electron transfer number was calculated by Koutecky-Levich (K-L) equation:

$$\frac{1}{J} = \frac{1}{J_k} + \frac{1}{J_L} = \frac{1}{J_k} + \frac{1}{B\omega^{1/2}} \quad (1)$$

$$B = 0.62nFC_0D_0^{2/3}\nu^{-1/6} \quad (2)$$

where J is the measured current density, J_k is the kinetic diffusion current density, J_L is the kinetic limiting current density, B is the reciprocal of the slope, ω is the angular velocity (ω=2πN, N is the rotation speed), n is transferred electron number, F is Faraday constant (96485 C mol^{-1}), C_0 is the saturated concentration of O_2 (1.2×10^{-6} mol cm^{-3}), D_0 is the diffusion coefficient of O_2 (1.9×10^{-5} cm^2 s^{-1}), and ν is the kinetic viscosity (0.01 cm^2 s^{-1}).

RRDE measurements were conducted to investigate the four-electron selectivity of the as-prepared samples. The H_2O_2 yield and electron transfer number (n) were calculated by the following equations:

$$H_2O_2(\%) = 200 \times \frac{I_r/N}{I_d + I_r/N} \quad (3)$$

$$n = 4 \times \frac{I_d}{I_d + I_r/N} \quad (4)$$

where I_d is the disk current, I_r is the ring current, and N is the current collection efficiency of the platinum ring (N=0.37).

The turnover frequency (TOF) was evaluated based on the mass content of Co/Fe (from ICP-OES results) to assume that all the Co/Fe sites were exposed and acted as the active sites for ORR. The equation is as follows:

$$TOF = \frac{J_k \times N_e}{W \times C_{cat} \times N_A / M} \quad (5)$$

where J_k is the kinetic current density (mA cm^{-2}) at a certain potential, N_e is the electron number per Coulomb (6.24×10^{18}), W is the metal content in the catalyst, C_{cat} is the catalyst loading on the electrode. N_A is the Avogadro constant (6.022×10^{23}), and M is molar mass of the metal (Fe: 55.845 g·mol^{-1}, Co: 58.933 g·mol^{-1}).

The ORR stability of the electrocatalysts in the O_2-staurated 0.1 M KOH solution was examined by accelerated deterioration tests (ADT) at a scan rate of 100 mV s^{-1} for 10,000 cycles between 0.6 and 1.1 V (vs. RHE). The ORR stability of the electrocatalysts was also performed by chronoamperometry at a potential of 0.80 V (vs. RHE) in O_2-staurated 0.1 M KOH. To test the tolerance to methanol, chronoamperometric measurements at 0.8 V (vs. RHE)

in a O_2-saturated 0.1 M KOH or 0.1 M $HClO_4$ solution along with the injection of methanol were performed. The methanol was added into the electrolyte at the time of 300 s.

Computational methods

All the density functional theory (DFT) calculations were performed using Vienna ab initio simulation package (VASP).[1] The generalized gradient approximation (GGA) with the Perdew-Burke-Ernzerh[2] of exchange correlation functional within the projector augmented wave method[3] was utilized to model the electron-ion interaction. An energy cutoff of 500 eV for the plane-wave basis set was used. The convergence threshold was set to 10^{-5} eV in energy and 0.02 eV/Å in force, respectively. To prevent the interaction between two neighboring images, the vacuum layer thickness was set to 20 Å. A semi-empirical van der Waals (vdW) correction proposed by Grimme (DFT-D3)[4] was included to account for the dispersion interactions.

The formation enegies (E_f) of various models for Co_2/Fe-N_{10} systems were calculated as follows:

$$E_f = E_{embedded} - E_{pure} + n_C\mu_C - n_N\mu_N - n_{Fe}\mu_{Fe} - n_{Co}\mu_{Co} - n_H\mu_H \quad (6)$$

where $E_{embedded}$ and E_{pure} are the total energies of nitrogen-coordinated Co-Co and/or Fe sites embedded carbon sheets, including the cases of pyridinic-N based, pyrrolic-N-based non-edged and edged models. The n_C is the reference energy of n_C removed C atoms from carbon sheet at a chemical potential of C atom (μ_C). The μ_N, n_{Fe}, n_{Co}, and n_H are the reference energies of n_{Fe}, n_{Co}, and n_H added Fe, Co and H atoms into carbon sheet at the chemical potentials of μ_N, μ_{Fe}, μ_{Co} and μ_H, respectively. ”

The free energy of each elementary step in the proton coupled electron transfer reactions was computed using the computational hydrogen electrode (CHE) model for oxygen reduction reaction (ORR). Considering the O_2 molecular is not broken before reduction, the associative $4e^-$ reduction pathway was evaluated to be most feasible for ORR in this work, as follows:

$$O_2 + * \rightarrow O_2* \quad (7)$$

$$O_2* + H_2O + e^- \rightarrow OOH* + OH^- \quad (8)$$

$$OOH* + e^- \rightarrow O* + OH^- \quad (9)$$

$$O* + H_2O + e^- \rightarrow OH* + OH^- \quad (10)$$

$$OH* + e^- \rightarrow OH^- + * \quad (11)$$

where * represents the active site on the corresponding surface.

The free energy of the reactants and each intermediate state at an applied electrode potential U are computed by the equation $\Delta G = \Delta E + \Delta ZPE - T\Delta S - neU$, where n is the electron number of such state and the ΔE was defined to be the difference of total energy of systems; ΔZPE and ΔS stand for the zero point energy change and entropy change which were determined by employing the computed vibrational frequencies and standard tables for the reactants and products in the gas phase. To avoid the poorly description of triplet state of O_2 in DFT calculations, the free energy of O_2(g) was evaluated to be $G_{O2} = 2G_{H2O} - 2G_{H2} - 4.92$ eV. The theoretical reaction overpotential (η_{ORR}) was evaluated to the difference between the minimum voltage needed for the ORR (1.23 V) and the voltage required for changing all the free-energy steps into downhill, which reads as:

$$\eta_{ORR} = 1.23 - \min(\Delta G_{1\text{-}4}) \quad (12)$$

where min ($\Delta G_{1\text{-}4}$) is the step with the smallest ΔG value in $\Delta G_{1\text{-}4}$.

Rechargeable Zn-air battery assembly and measurements

The home-made Zn-air batteries (ZABs) were assembled by using polished zinc foil as the anode and aqueous solution containing 6 M KOH+0.2 M zinc acetate as the electrolyte. Co_2/Fe-N@CHC or commercial Pt/C coated on carbon paper was used as the air cathode. The total catalyst loading amount on carbon paper was 2.0 mg cm^{-2} for both Co_2/Fe-N@CHC and commercial Pt/C. The discharge/charge polarization curves were measured using CHI 760E electrochemical workstation. For cycling stability test, the ZABs based on Co_2/Fe-N@CHC+RuO_2 (with a mass ration of 1:1) and Pt/C+RuO_2 (with a mass ration of 1:1) were also assembled. The galvanostatic discharge/charge cycling stability for the ZABs was performed using a Neware battery testing station system (CT-3008) with a cycling interval of 40 min (20 min for discharging and 20 min for charging) under ambient condition.

Supplementary Figures and Tables

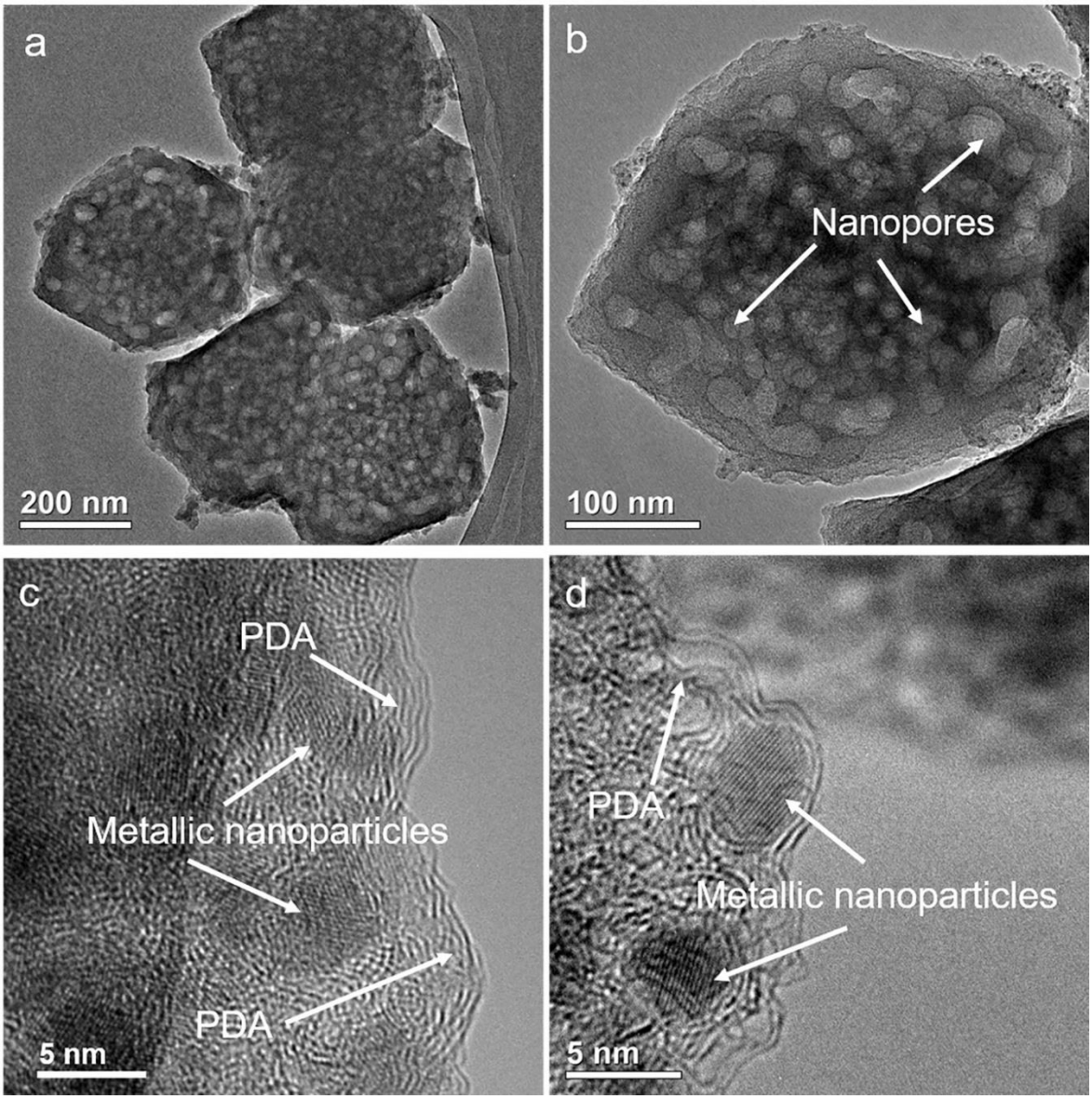

Figure S1. (a, b) TEM images of CoFe-DOPA@ZIF-8, (c, d) HRTEM images of CoFe-DOPA@ZIF-8.

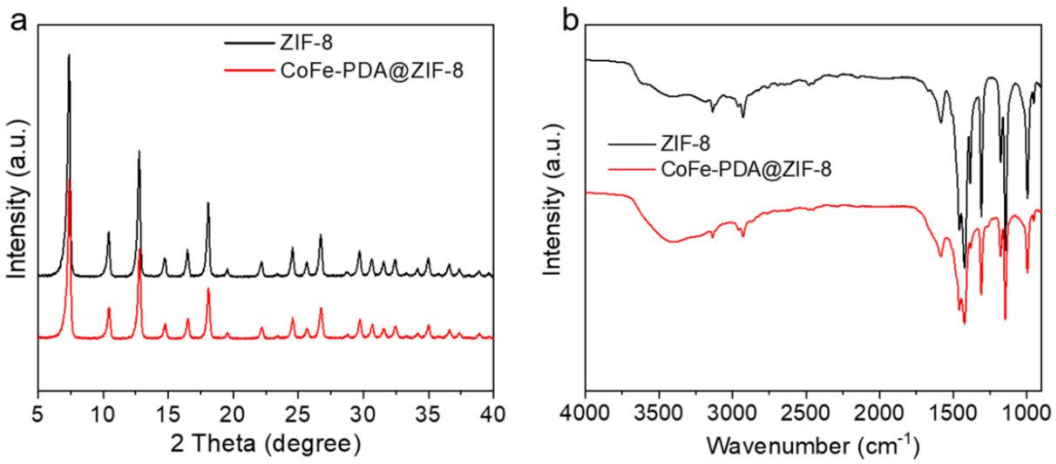

Figure S2. (a) XRD patterns, (b) FTIR spectra of ZIF-8 and CoFe-PDA@ZIF-8.

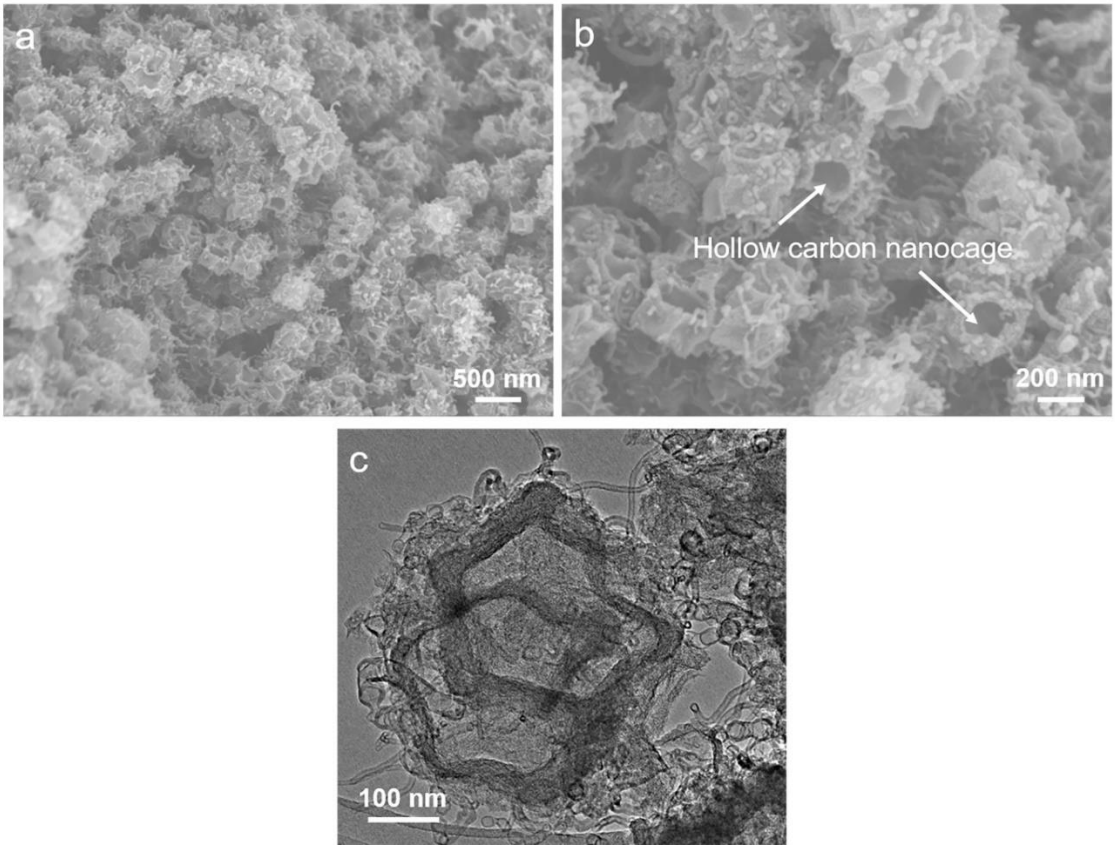

Figure S3. (a, b) SEM images, and (c) TEM image of Co_2/Fe-N@CHC.

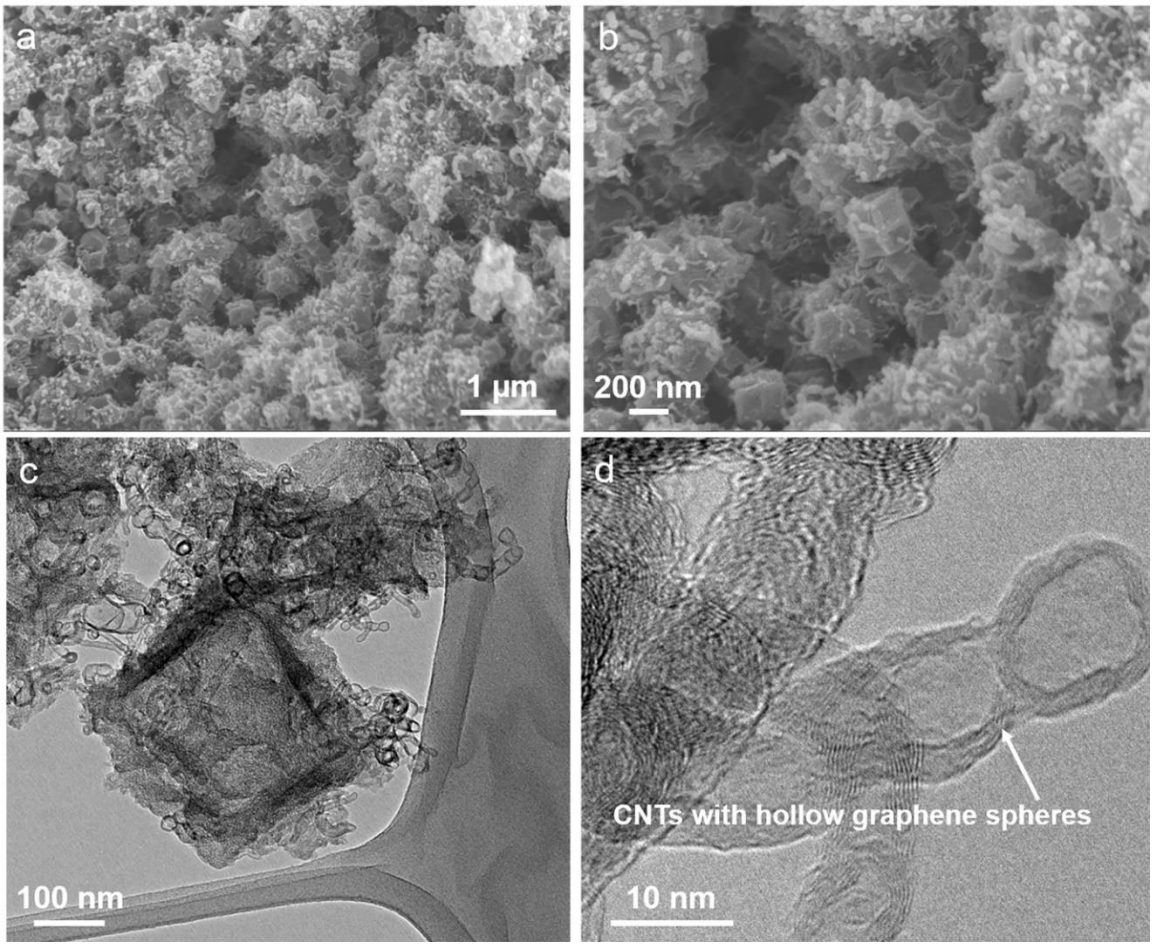

Figure S4. (a, b) SEM images of CoFe NPs@CHC, (c) TEM images of CoFe NPs@CHC, (d) HRTEM images of CoFe NPs@CHC.

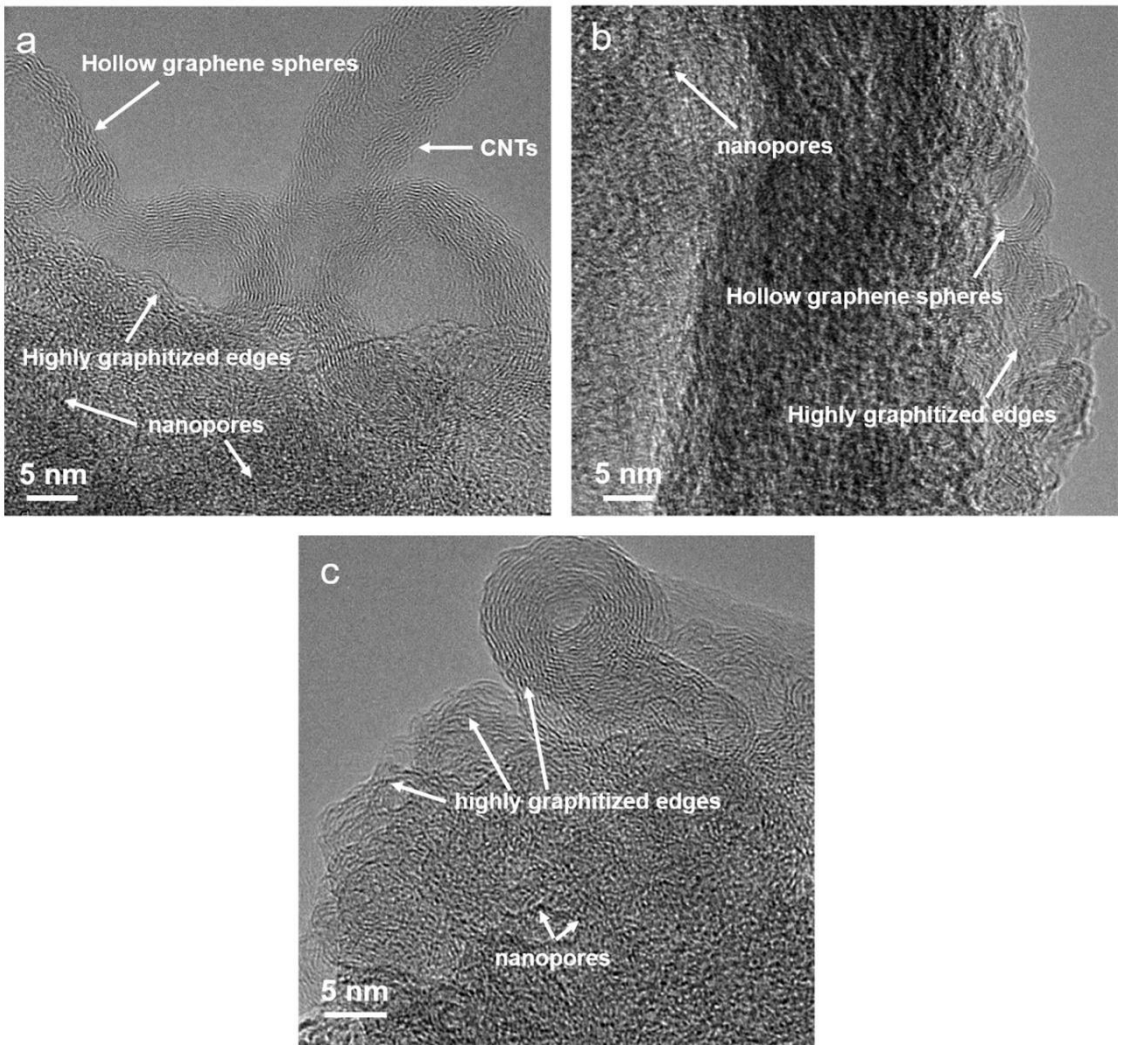

Figure S5. HRTEM images of Co_2/Fe-N@CHC.

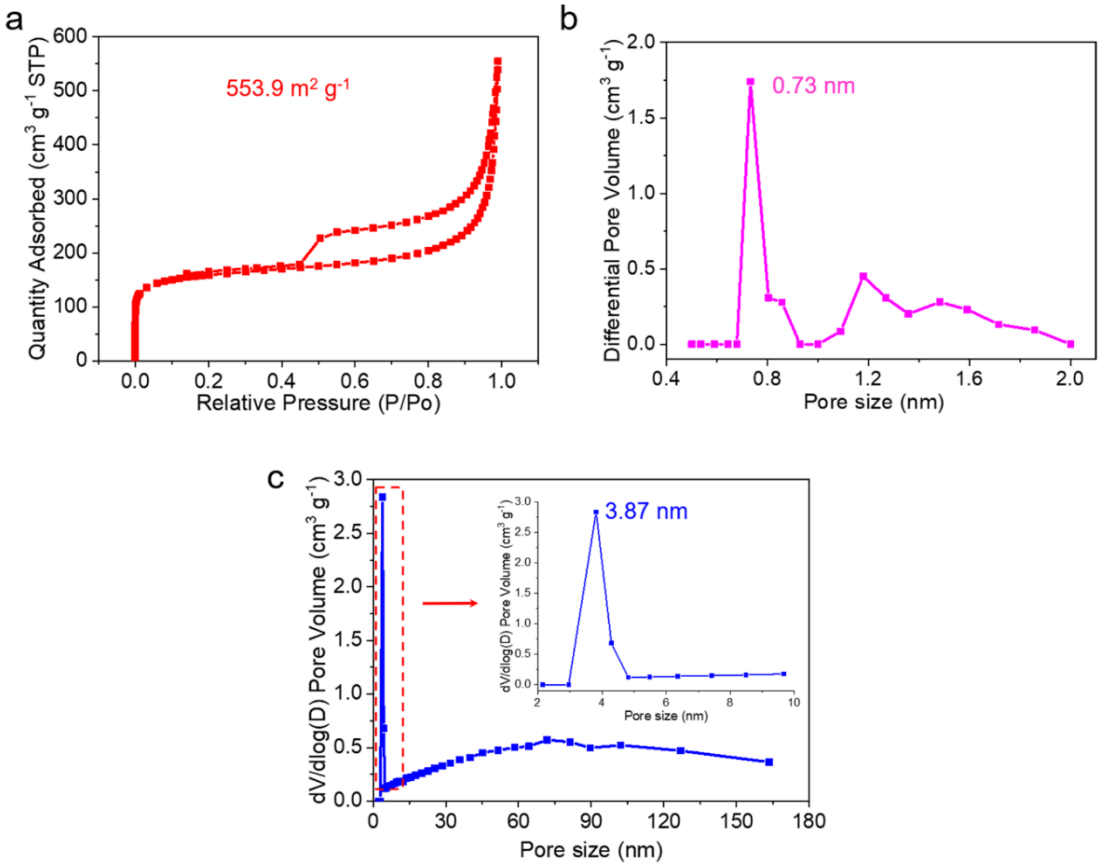

Figure S6. (a) N_2 adsorption-desorption isotherms of Co_2/Fe-N@CHC, (b, c) the corresponding pore size distribution.

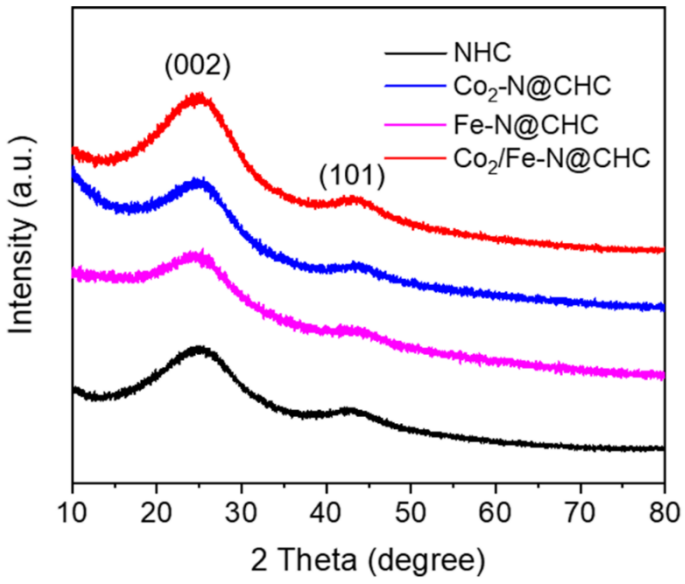

Figure S7. XRD patterns of NHC, Co_2-N@CHC, Fe-N@CHC, and Co_2/Fe-N@CHC.

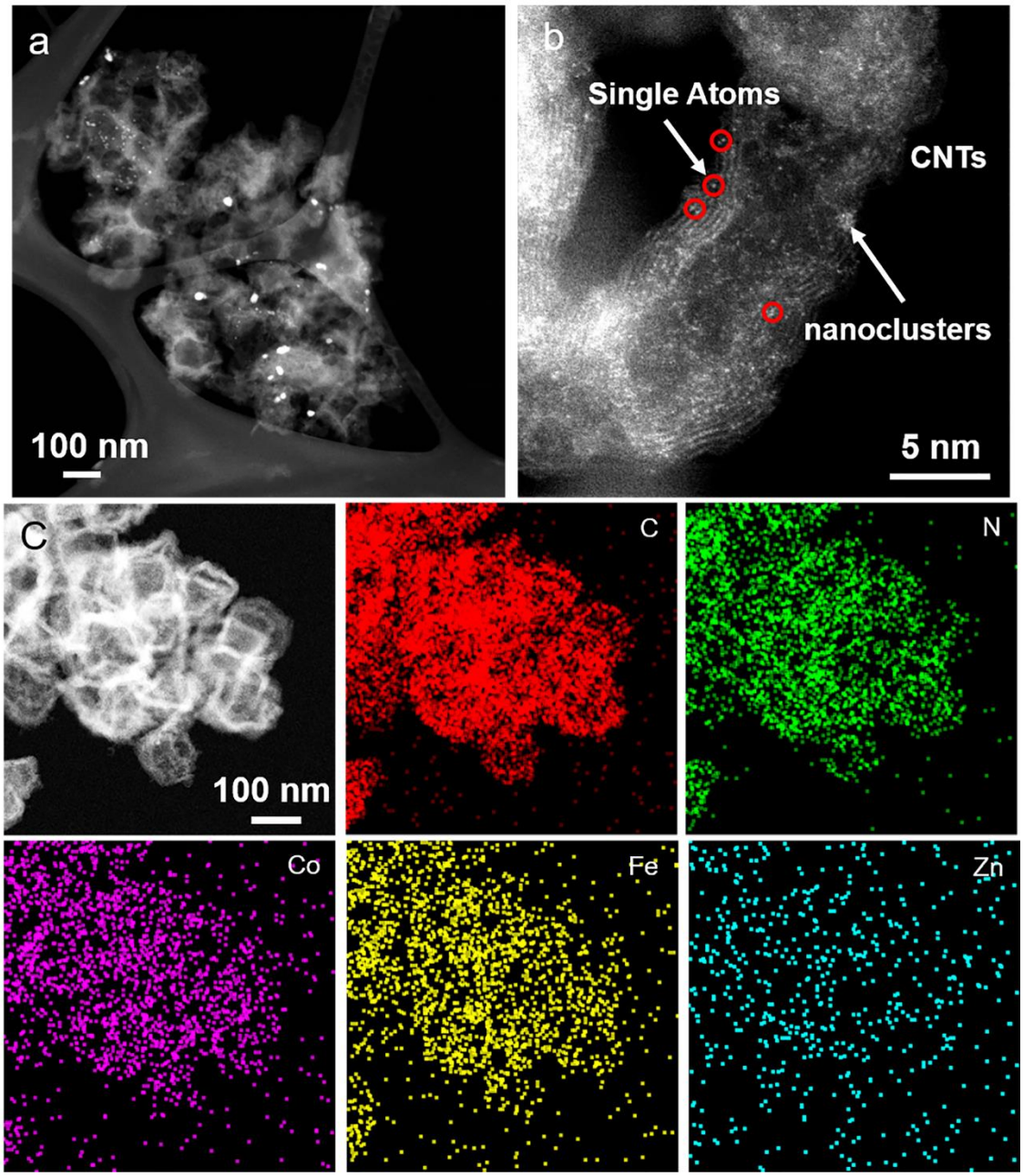

Figure S8. (a, b) Aberration-corrected HAADF-STEM images, and (c) HAADF-STEM image and corresponding elemental maps (C: red, N: green, Co: pink, and Fe: yellow, Zn: cyan) of CoFe NPs@CHC.

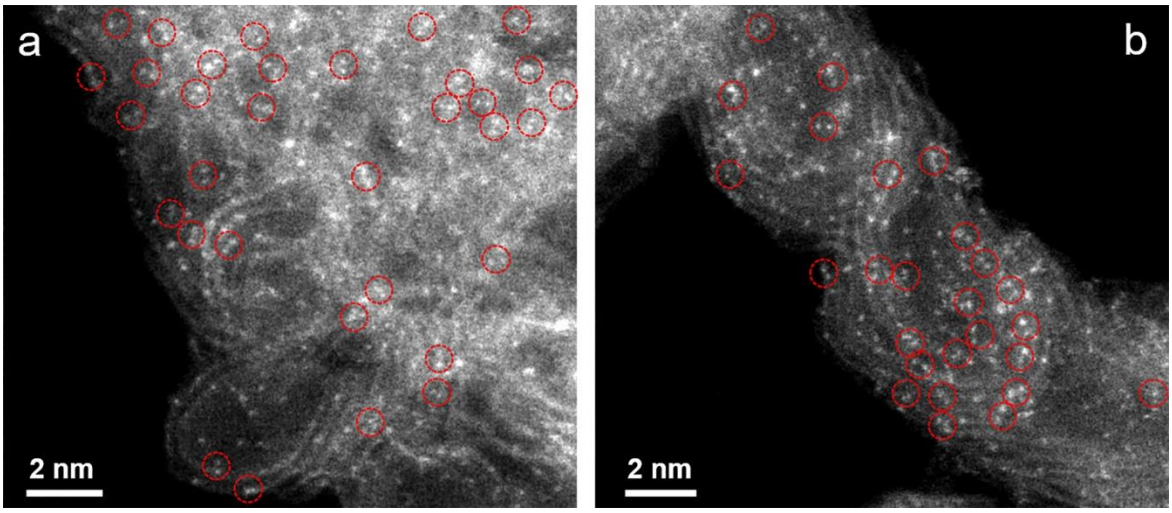

Figure S9. (a, b) Magnified AC HAADF-STEM image of Co_2/Fe-N@CHC.

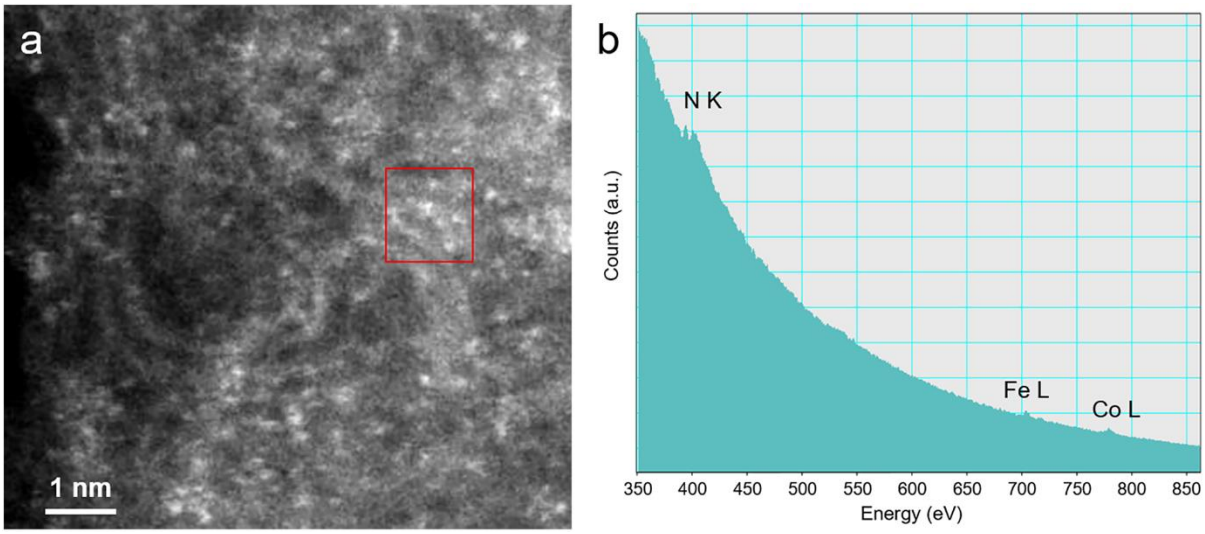

Figure S10. (a) AC HAADF-STEM image of Co_2/Fe-N@CHC, (b) the cooresponding EELS analysis of the selected region in (a) that contains both single spots (Fe atoms) and paired spots (Co-Co dimers).

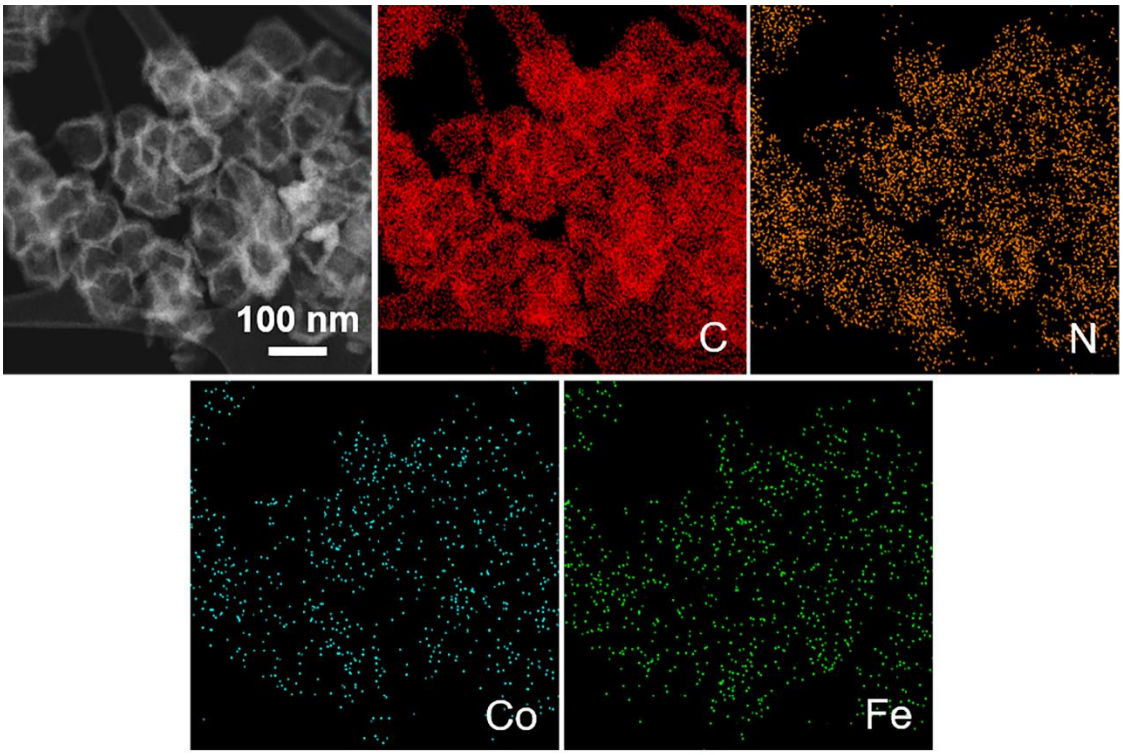

Figure S11. HAADF-STEM image and corresponding elemental maps (C: red, N: orange, Co: cyan, and Fe: green) of Co_2/Fe-N@CHC.

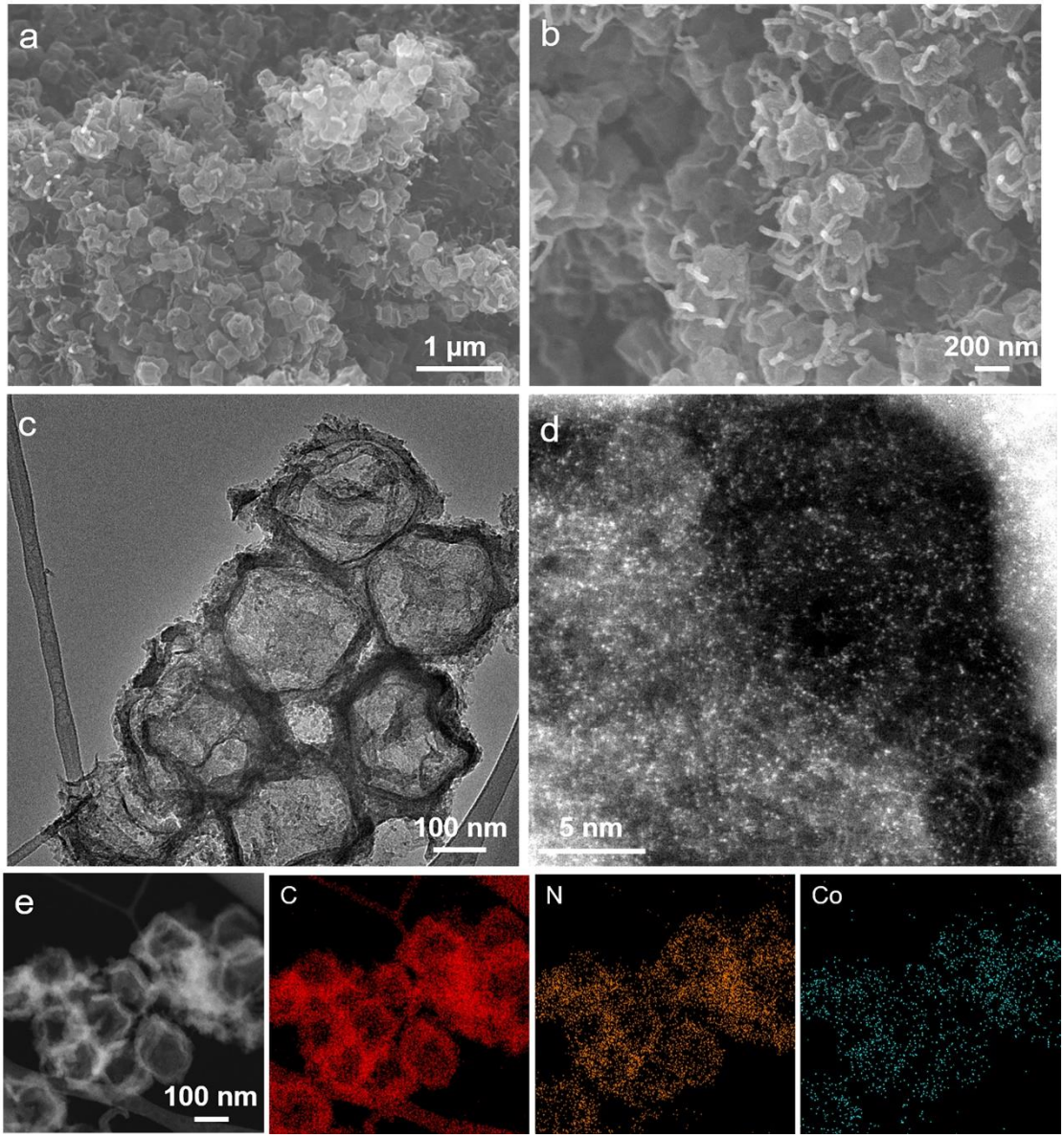

Figure S12. (a, b) SEM images of Co_2-N@CHC, (c) TEM image of Co_2-N@CHC, (d) Aberration-corrected HAADF-STEM image of Co_2-N@CHC, (e) HAADF-STEM image and corresponding element maps of Co_2-N@CHC.

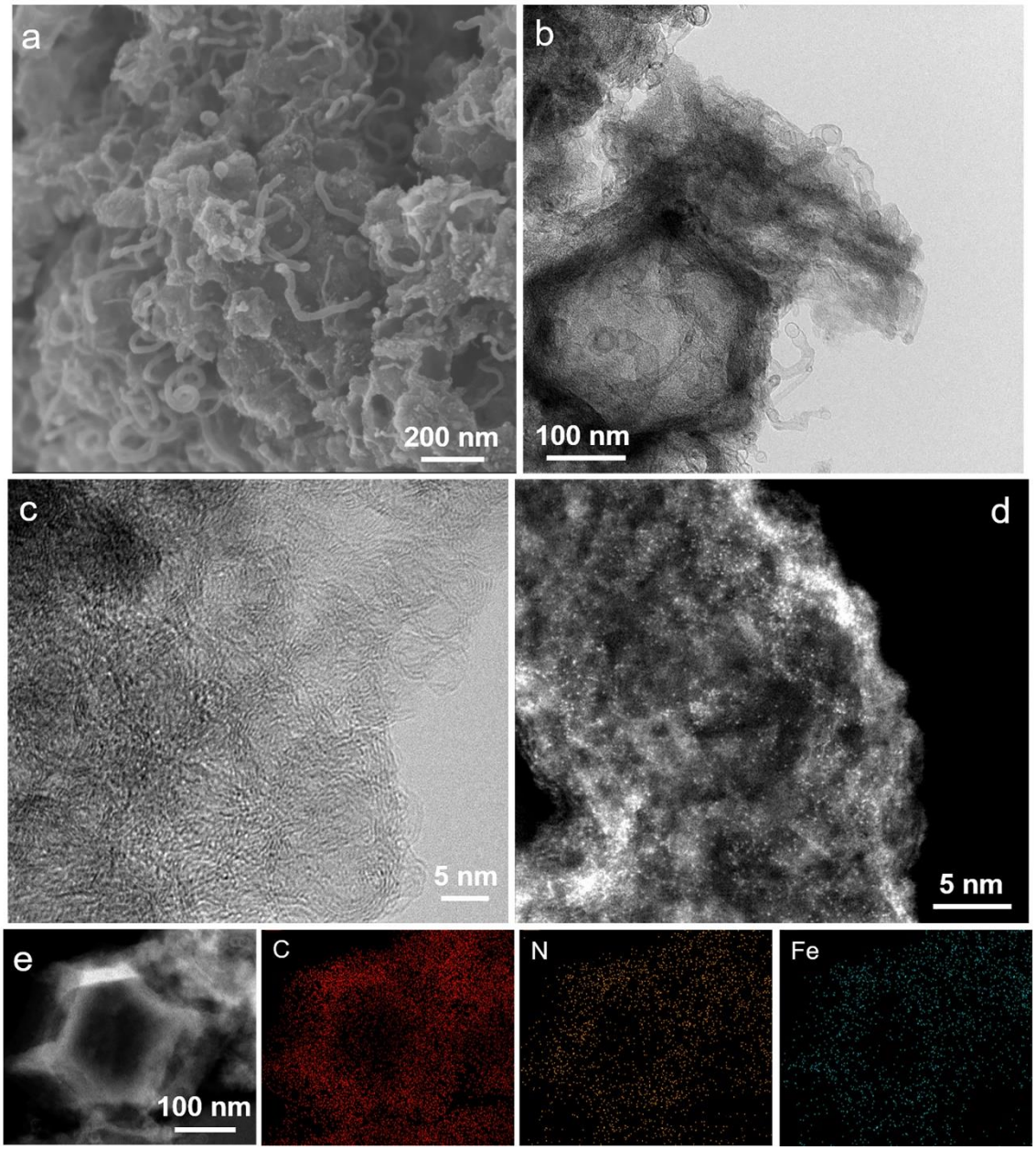

Figure S13. (a, b) SEM images of Fe-N@CHC, (c) HRTEM image of Fe-N@CHC, (d) Aberration-corrected HAADF-STEM image of Fe-N@CHC, (e) HAADF-STEM image and corresponding element maps (C: red, N: orange, Co: cyan) of Fe-N@CHC.

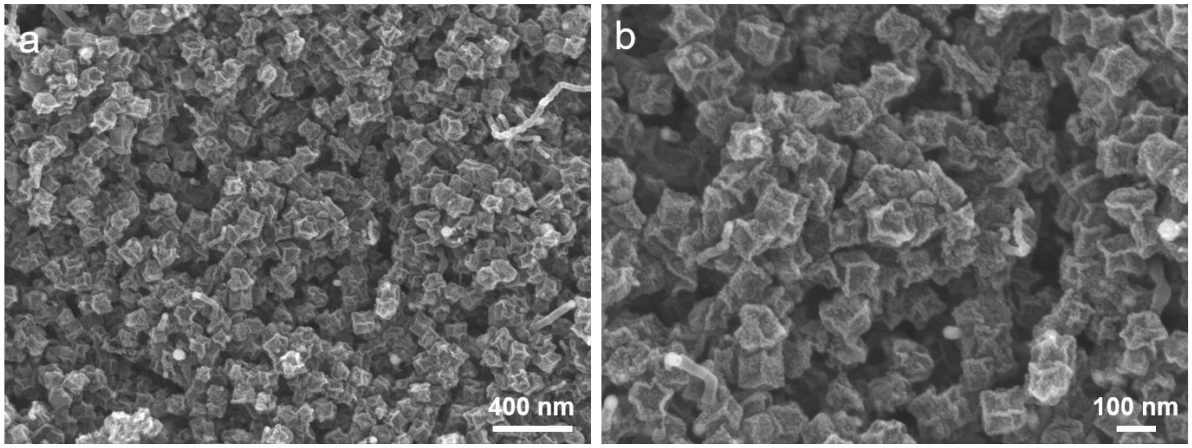

Figure S14. (a, b) SEM images of NHC.

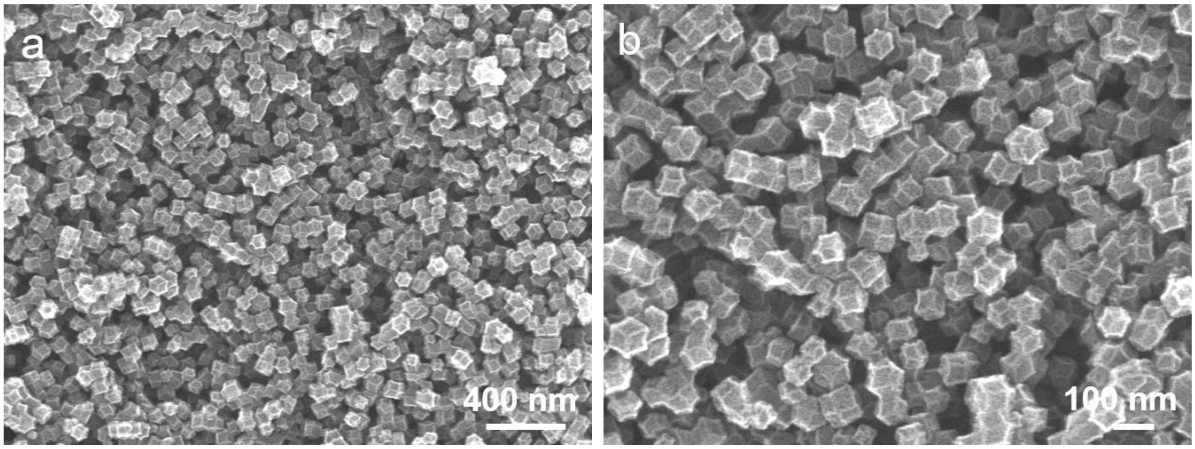

Figure S15. (a, b) SEM images of pyrolyzed ZIF-8.

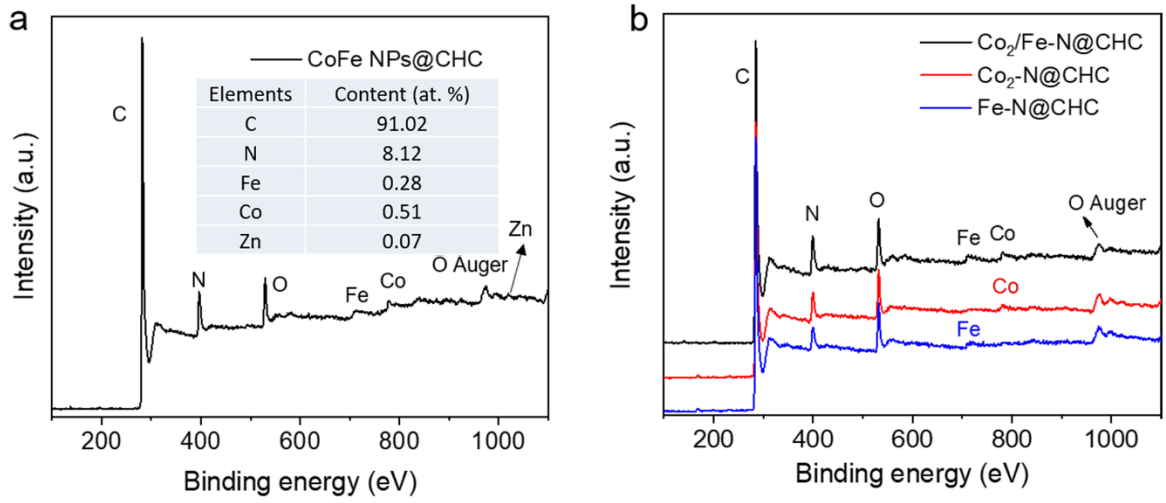

Figure S16. The XPS survey spectra of (a) CoFe NPs@CHC, (b) Co_2/Fe-N@CHC, Co_2-N@CHC, and Fe-N@CHC.

Table S1. Element contents determined by XPS and ICP-OES.

Catalyst materials	XPS				Co (wt. %) ICP-OES	Fe (wt. %) ICP-OES
	C (at. %)	N (at. %)	Co (at. %) Co (wt. %)	Fe (at. %) Fe (wt. %)		
Co_2-N@CHC	91.92	7.51	0.57 2.70	-	2.87	-
Fe-N@CHC	93.10	6.39	-	0.51 2.31	-	2.52
Co_2/Fe-N@CHC	91.77	7.63	0.41 1.94	0.19 0.85	2.13	0.98

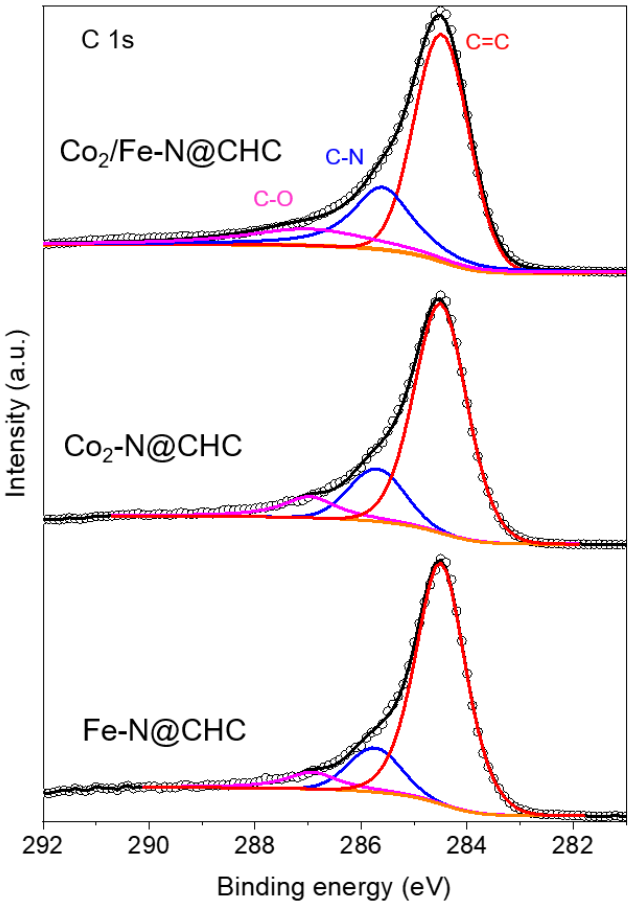

Figure S17. The C 1s XPS spectra of Co_2/Fe-N@CHC, Co_2-N@CHC, and Fe-N@CHC.

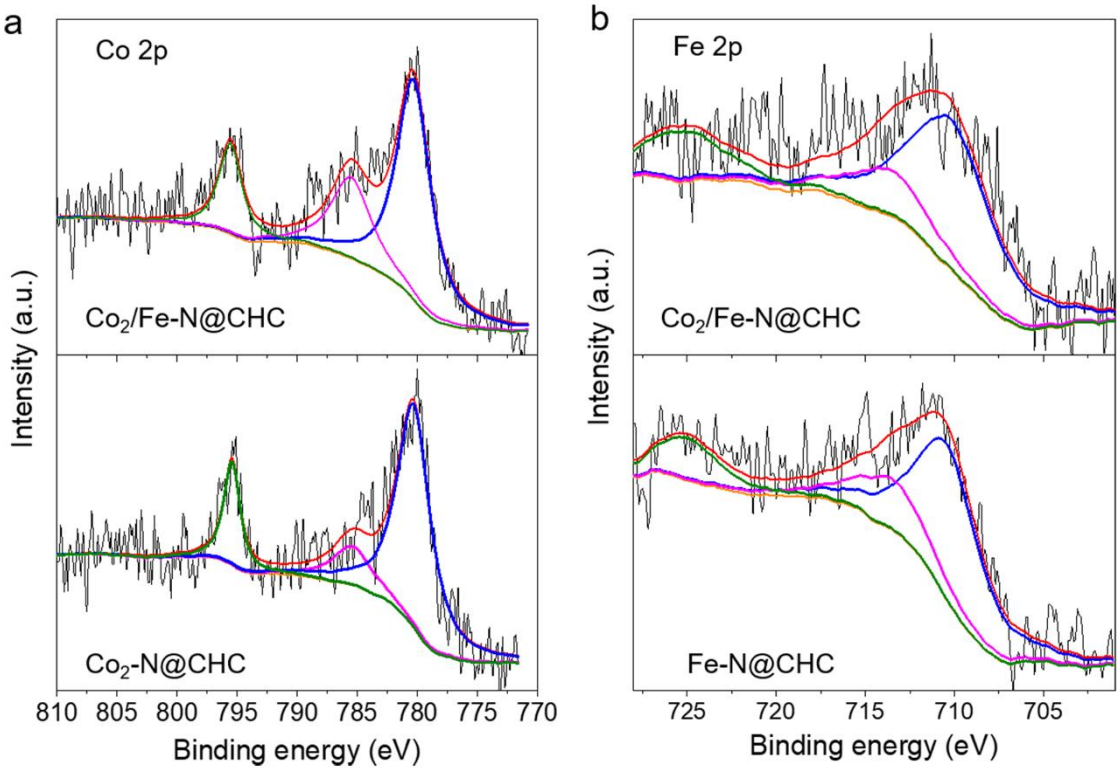

Figure S18. (a) The Co 2p XPS spectra of Co_2/Fe-N@CHC and Co_2-N@CHC, (b) The Fe 2p XPS spectra of Co_2/Fe-N@CHC and Fe-N@CHC.

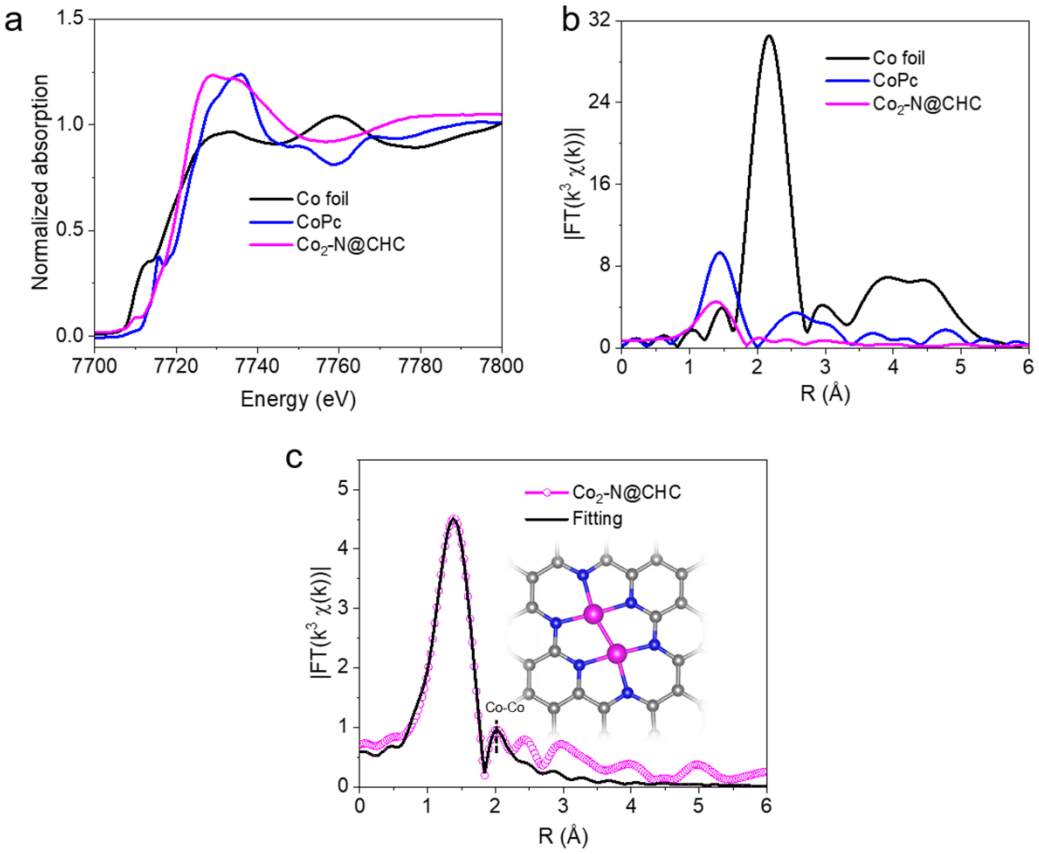

Figure S19. (a) XANES Co K-edge spectra, (b) Co K-dege k^3-weighted Fourier transform (FT) spectra of Co_2-N@CHC in comparison with Co foil and CoPc samples, respectively, (c) The extended X-ray absorption fine structure (EXAFS) R space fitting curves of Co_2-N@CHC.

Table S2. The Co K-edge EXAFS curves fitting parameters of Co_2/Fe-N@CHC and Co_2-N@CHC, and the Fe K-edge EXAFS curves fitting parameters of Co_2/Fe-N@CHC and Fe-N@CHC.

Sample	Bonding pair	CN	R (Å)	e_0	σ^2 ($Å^2$ x 10^{-3})
Co_2/Fe-N@CHC	Co-N	3	1.842	-0.38	7.75
	Co-Co	1	2.406	-1.22	10.2
Co_2/Fe-N@CHC	Fe-N	4	1.960	0.68	10.6
Co_2-N@CHC	Co-N	3	1.843	-0.51	7.99
	Co-Co	1	2.410	1.12	9.98
Fe-N@CHC	Fe-N	4	1.980	1.93	10.7

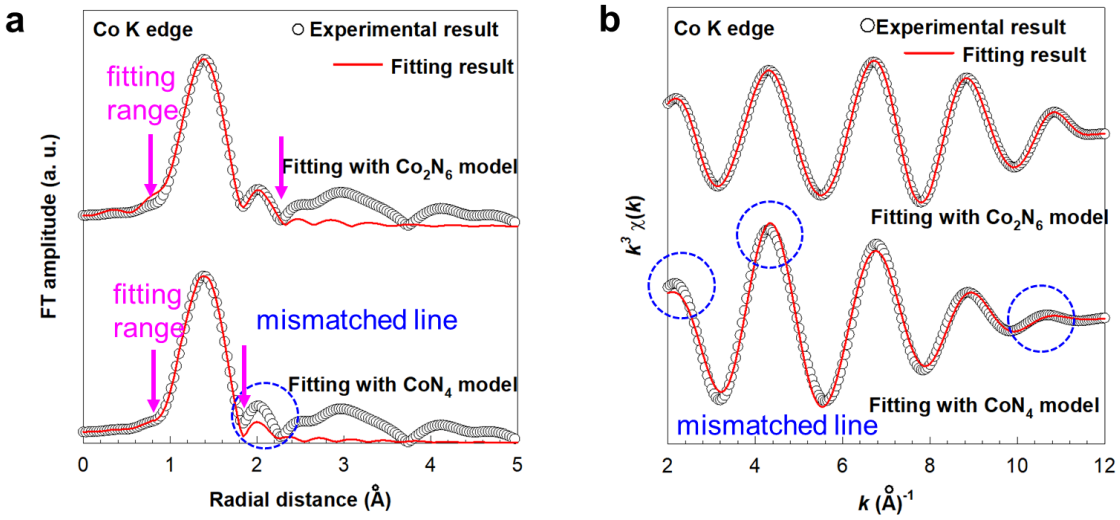

Figure S20. (a) Experimental and fitted Co K edge FT-EXAFS spectra of Co_2/Fe-N@CHC based on Co_2N_6 and CoN_4 structural models and (b) the corresponding Fourier filtered EXAFS spectra. The arrows represent the R range employed for curve fitting analysis.

As shown in Figure S20, the FT-EXAFS and Fourier filtered EXAFS spectra of Co_2/Fe-N@CHC could not be well reproduced with monomeric CoN_4 model, as highlighted in blue circles. This is in stark contrast to the good fits obtained with dimeric Co_2N_6 model. These results allow us to further conclude that the Co_2/Fe-N@CHC catalyst contains Co_2N_6 units (Co-Co sites) rather than Co-N_4 units.

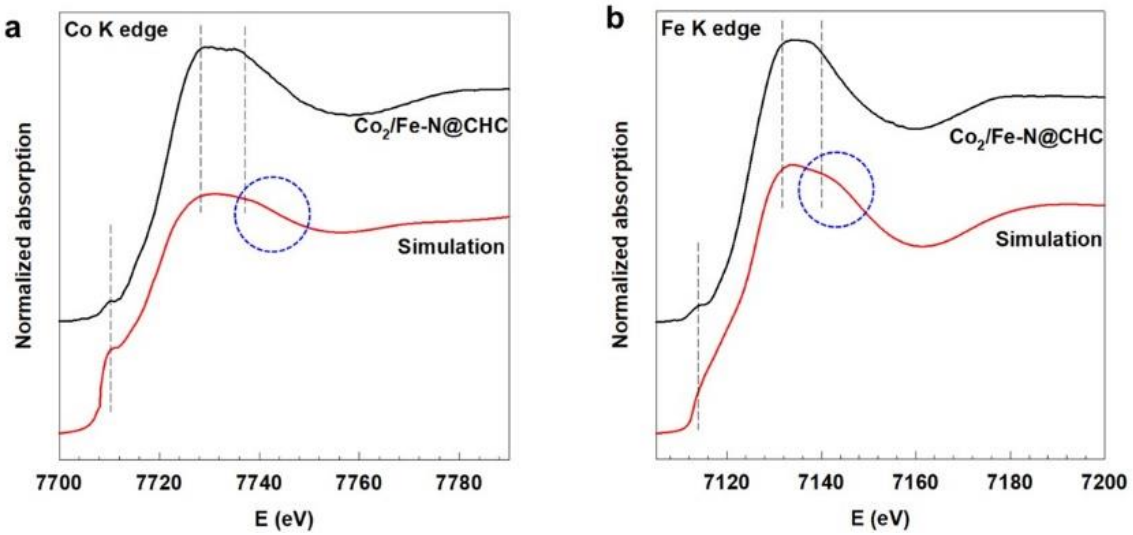

Figure S21. (a) Experimental and simulated Co K-edge XANES spectra, (b) Experimental and simulated Fe K-edge XANES spectra.

As depicted in Figure S21a, a high level of consistency could be obtained between experimental and simulated Co K-edge XANES spectra with dimeric Co_2N_6 model. Meanwhile, a high level of consistency between the experimental and simulated Fe K-edge XANES spectra with monomeric FeN_4 model could also be obtained (Figure S21b). The inspection revealed that the presence of dimeric Co-Co pair leads to the broadening of intense resonance peak at ~7730 eV in the Co K-edge XANES spectrum (as highlighted in blue circle), which is distinguishable from the less broad resonance peak at ~7130 eV in the Fe K-edge XANES spectrum with monomeric FeN_4 structure.

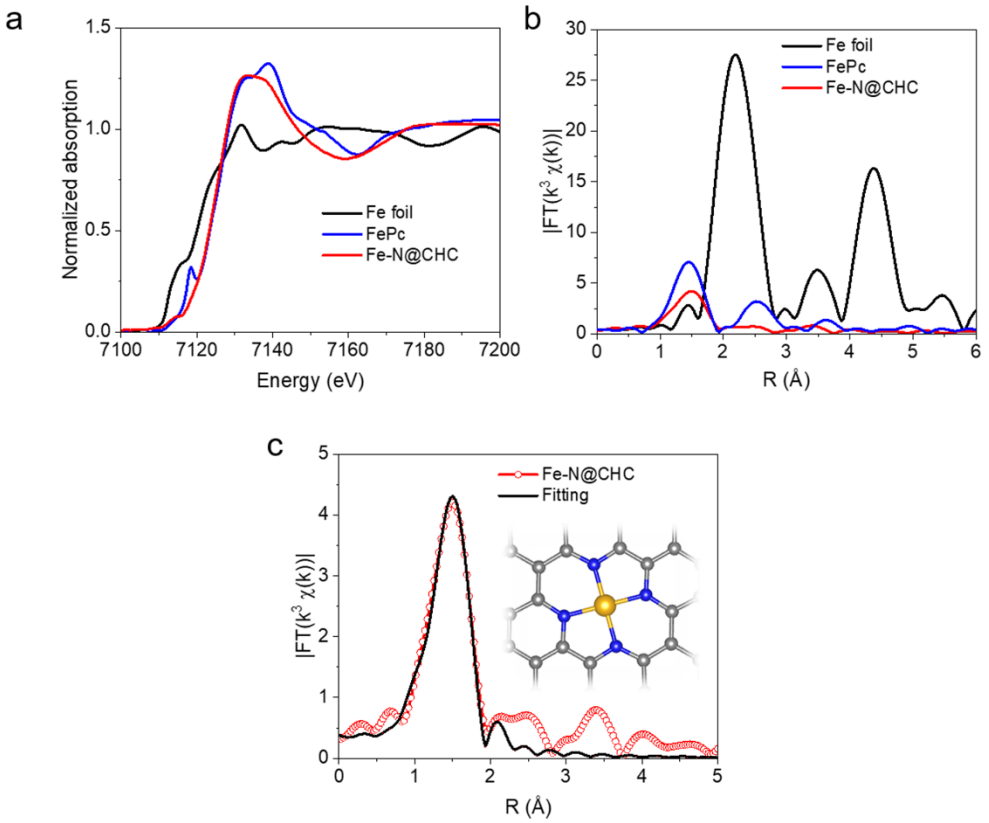

Figure S22. (a) XANES Fe K-edge spectra, (b) Fe K-dege k^3-weighted Fourier transform (FT) spectra of Fe-N@CHC in comparison with Fe foil and FePc samples, respectively, (c) The extended X-ray absorption fine structure (EXAFS) R space fitting curves of Fe-N@CHC.

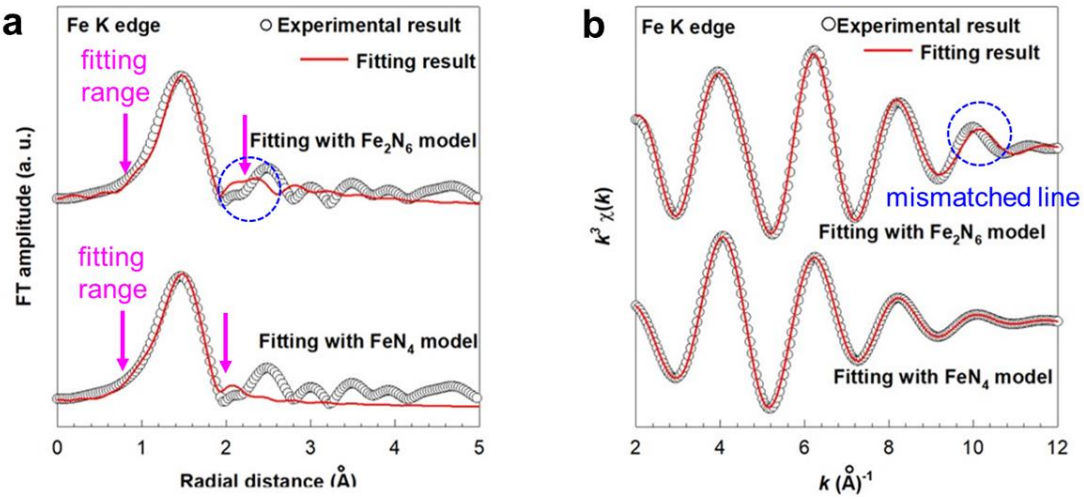

Figure S23. (a) Experimental and fitted Fe K edge FT-EXAFS spectra of Co_2/Fe-N@CHC based on Fe_2N_6 and FeN_4 structural models and (b) the corresponding Fourier filtered EXAFS spectra. The arrows represent the R range employed for curve fitting analysis.

Table S3. The Co K-edge and Fe K-edge EXAFS curve fitting parameters of Co_2/Fe-N@CHC with several structural models.

Structural model	Bonding pair	CN	R(Å)	e0	σ^2 (Å $\times 10^{-3}$)
Monomeric FeN_4 model	Fe–N	4	1.960	0.68	10.6
Dimeric Fe_2N_6 model	Fe–N Fe–Fe	3 1	1.961 2.620	-1.34 14.58	8.99 24.0

* The unreasonable fitting parameters are highlighted with yellow background.

As shown in Figure S23a, the FT-EXAFS spectrum of Co_2/Fe-N@CHC could not be reproduced with this dimeric model for the given R range (especially for the peak at ~2.2 Å, as highlighted by circle), clearly demonstrating the absence of (Fe-Fe) coordination shell. The poor fit obtained with the Fe_2-N_6 structural model was further evidenced by the inconsistency between experimental and calculated Fourier-filtered spectra, as highlighted by circles (Figure S23b). Additionally, as presented in Table S3, the EXAFS fitting analysis with this Fe_2N_6 structural model gave unreasonably large e_0 value for (Fe-Fe) coordination shell and huge Debye-Waller factor. Since such abnormal e_0 value (larger/lower than +5/-5 eV) and very large Debye-Waller factor prove the poor relevancy of EXAFS fitting result with the dimeric model, the obtained fitting results can be regarded as another evidence for the absence of (Fe-Fe) bonding pair. In contrast to this dimeric model, the monomeric FeN_4 model only with (Fe-N) coordination shell gave a reasonable fit for the experimental spectrum in the R range of 0.982~2.117 Å (Figure S23a). Such EXAFS fitting analysis provided additional support for the presence of Fe-N_4 unit without the (Fe-Fe) moiety.

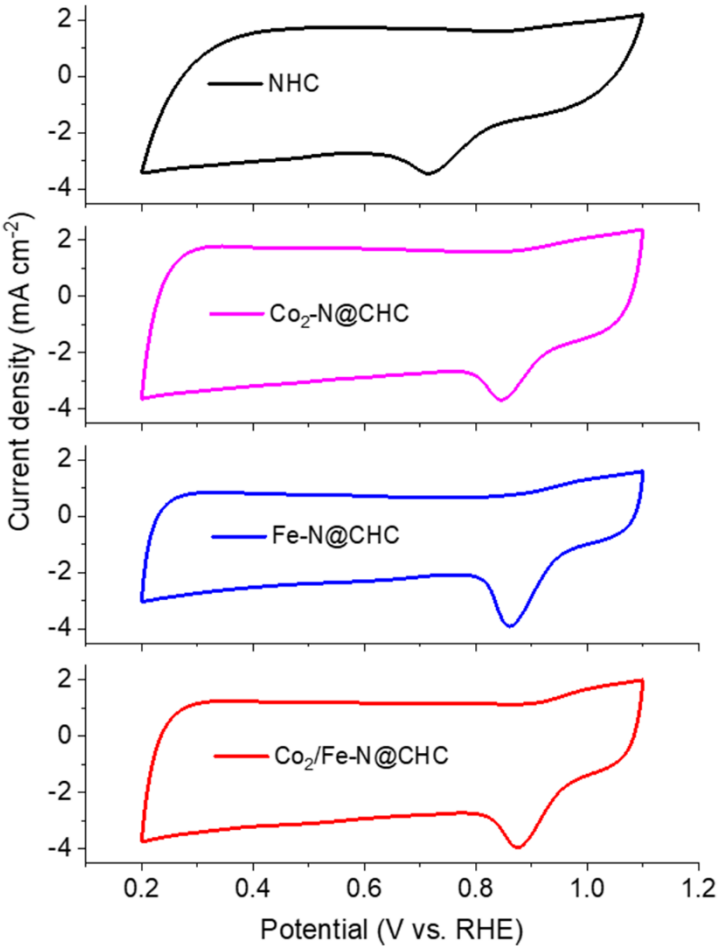

Figure S24. CV curves of NHC, Co_2-N@CHC, Fe-N@CHC, and Co_2/Fe-N@CHC in O_2-staurated 0.1 M KOH at a scan rate of 50 mV/s.

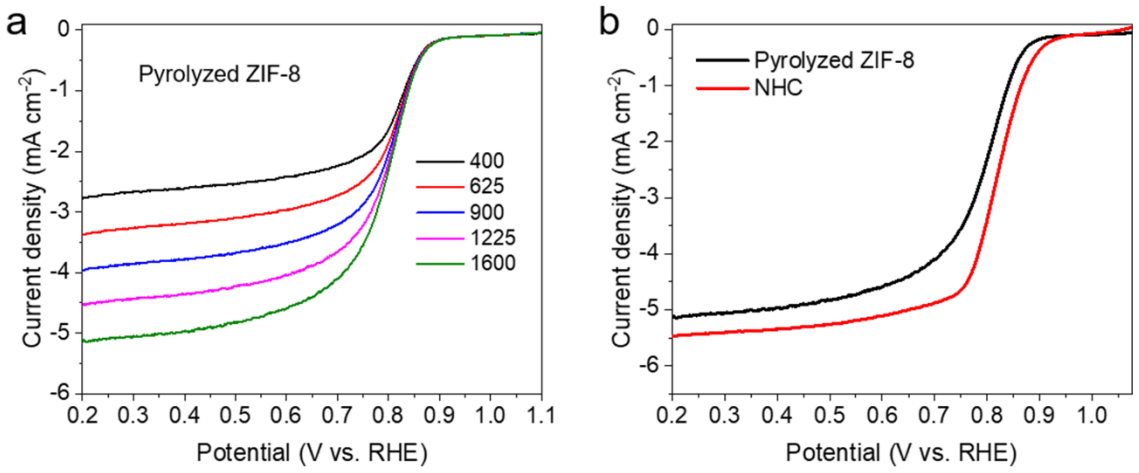

Figure S25. (a) LSV curves of pyrolyzed ZIF-8 at different rotating rates. (b) LSV curves of pyrolyzed ZIF-8, and NHC in O_2-staurated 0.1 M KOH solution at 1600 rpm.

Table S4. Comparison of the ORR performance between Co_2/Fe-N@CHC and state of the art other catalysts reported in the literatures in 0.1 M KOH solution.

Electrocatalysts	Onset potential (V vs. RHE)	Half-wave potential ($E_{1/2}$ V vs. RHE)	J_k (mA cm^{-2})	Reference
Co_2/Fe-N@CHC	1.03	0.915	9.44 @0.90 V	This work
Co-pyridinic N-C	0.99	0.87	-	Adv. Energy Mater. **2020**, 2002592
Mg-N-C	1.03	0.910	-	Nat. Commun. **2020**, 11, 938.
Fe-NC-S	-	0.88	~2 @0.90 V	Chem **2020,** 6, 1–15
Fe-N/P-C-700	0.941	0.867	-	J. Am. Chem. Soc. **2020**, 142, 2404.
FeCu-DA/NC	0.96	0.86 V	1.87 @0.90 V	J. Mater. Chem. A. **2020**, 8, 16994-7001.
Co SAs/3D GFs	1.03	0.901	5 @0.85 V	Angew. Chem. **2020**, 132, 20645 –20649
*pf*SAC-Fe-0.2	1.01	0.910	25.86 @0.85 V	Sci. Adv. **2019**, 5, eaaw2322.
Zn/CoN-C	1.004	0.861	-	Angew. Chem. Int. Ed. **2019**, 58,2622–2626.
Fe-NC SAC	0.98	0.90	-	Nat. Commun. **2019**, 10, 1278
Fe-N-C HNSs	1.046	0.87	-	Adv. Mater. **2019**, 31, 180631
Fe-NCNWs	-	0.91	6.0 @0.90 V	ACS Catal. **2019**, 9, 5929–5934.
Cu-SAs/N-C	~1	0.895	-	Nat. Catal. **2018**, 1, 781– 786.
Fe-SAs/NPS-HC	1.02	0.912 V	71.9 @0.85 V	Nat. Comm. **2018**, 9, 5422.
SA-Fe/NG	1.0	0.88	-	PNAS **2018**, 115, 6626–6631.
Fe-N_4 SAs/NPC	0.972	0.885	-	Angew.Chem. Int.Ed. **2018**, 57,8614 –8618
Fe ISAs/CN	0.986	0.90	37.83 @0.85V	Angew. Chem., Int. Ed. **2017**, 56, 6937
Co SAs/N-C(900)	0.982	0.881	~21 @0.80 V	Angew. Chem., Int. Ed. **2016**, 128, 10958 –10963

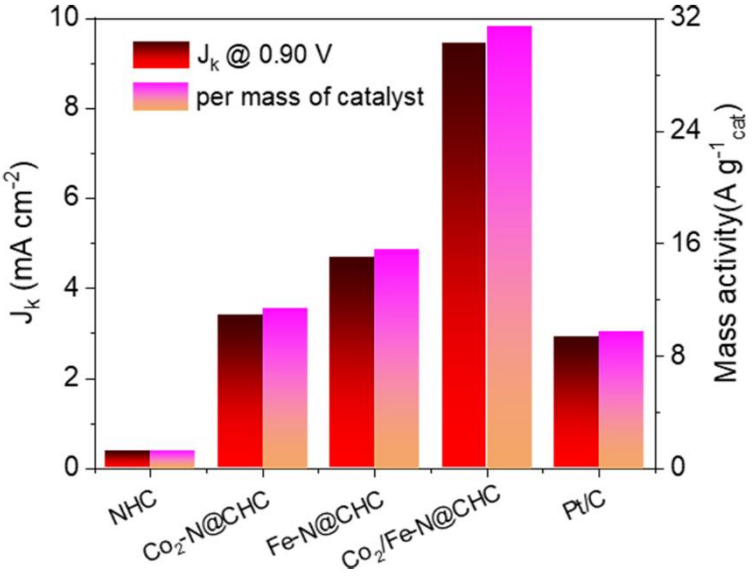

Figure S26. J_k and mass activity for Co_2/Fe-N@CHC, Fe-N@CHC, Co_2-N@CHC, NHC, and Pt/C are calculated by the total mass of the catalyst at 0.9 V (vs. RHE).

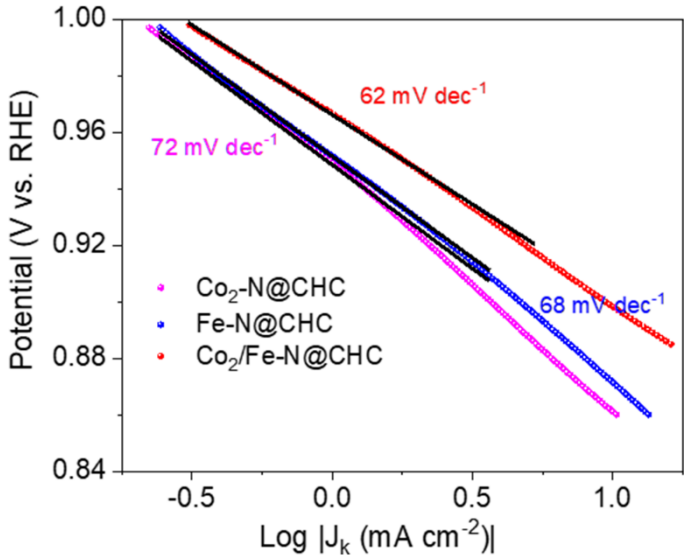

Figure S27. Tafel slops for Co_2-N@CHC, Fe-N@CHC, and Co_2/Fe-N@CHC.

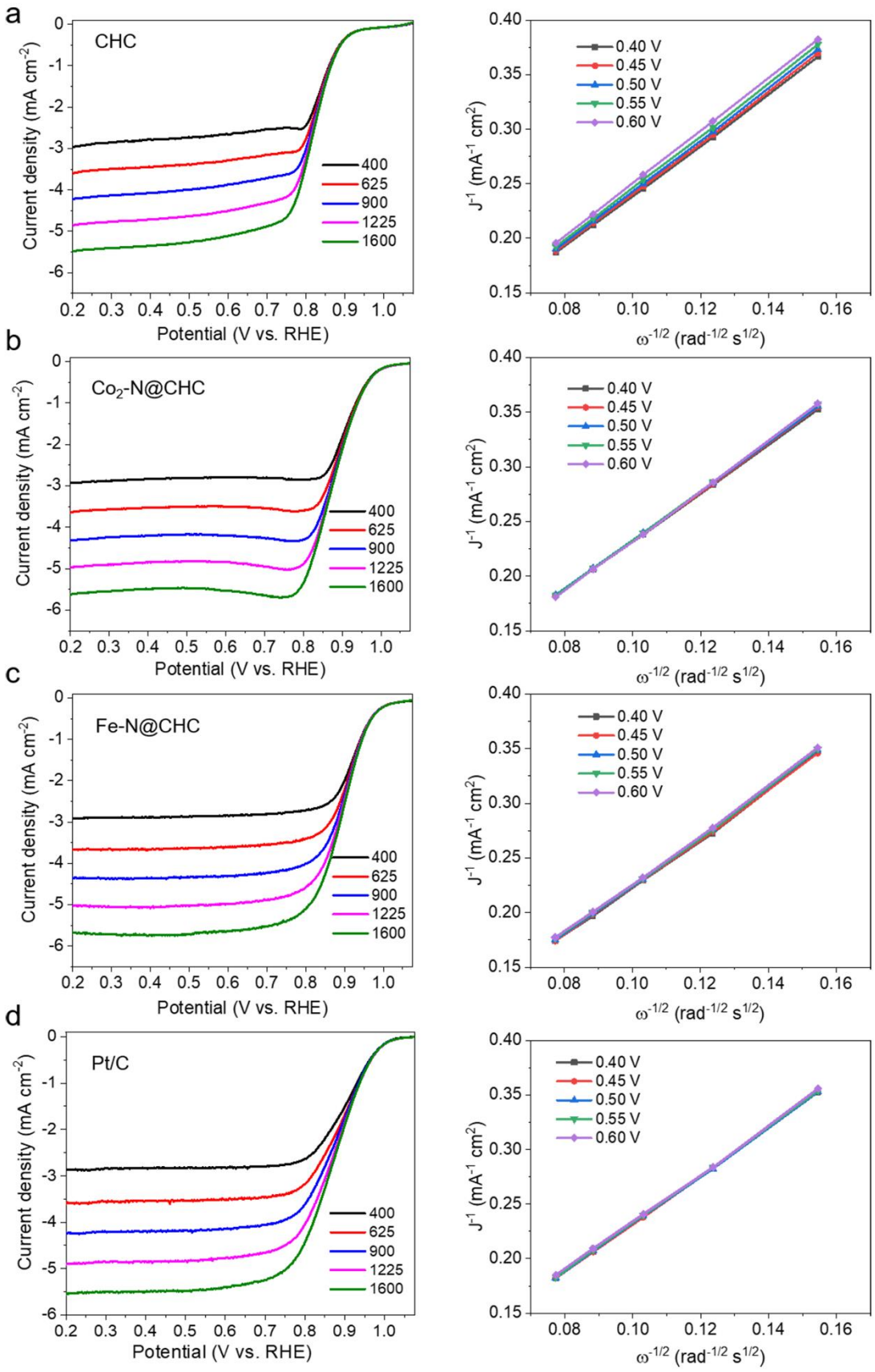

Figure S28. LSV curves of (a) NHC, (b) Co_2-N@CHC, (c) Fe-N@CHC, and (d) Pt/C at different rotating rates and the corresponding K-L plots.

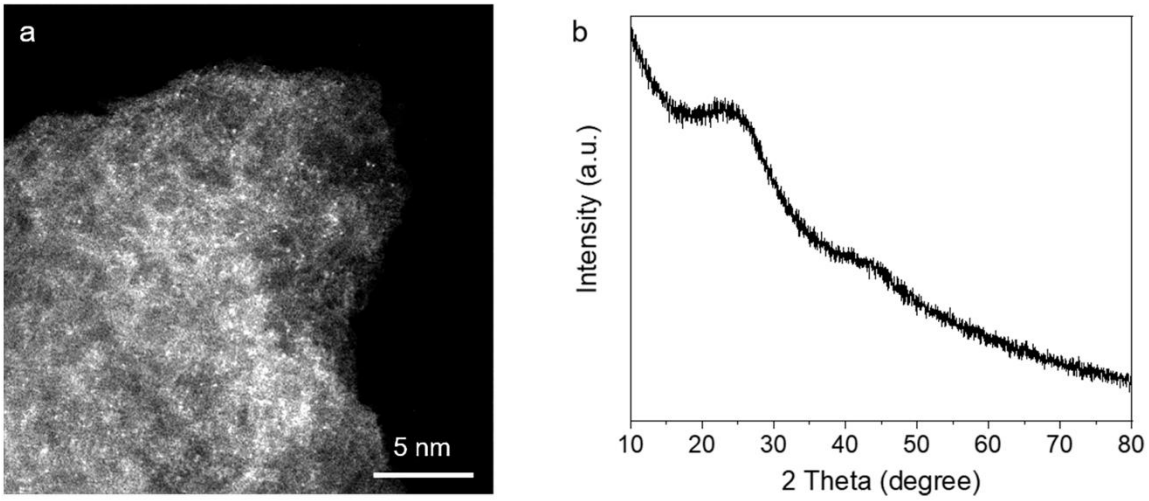

Figure S29. (a) HAADF-STEM image of Co_2/Fe-N@CHC after stability test, (b) the corresponding XRD pattern.

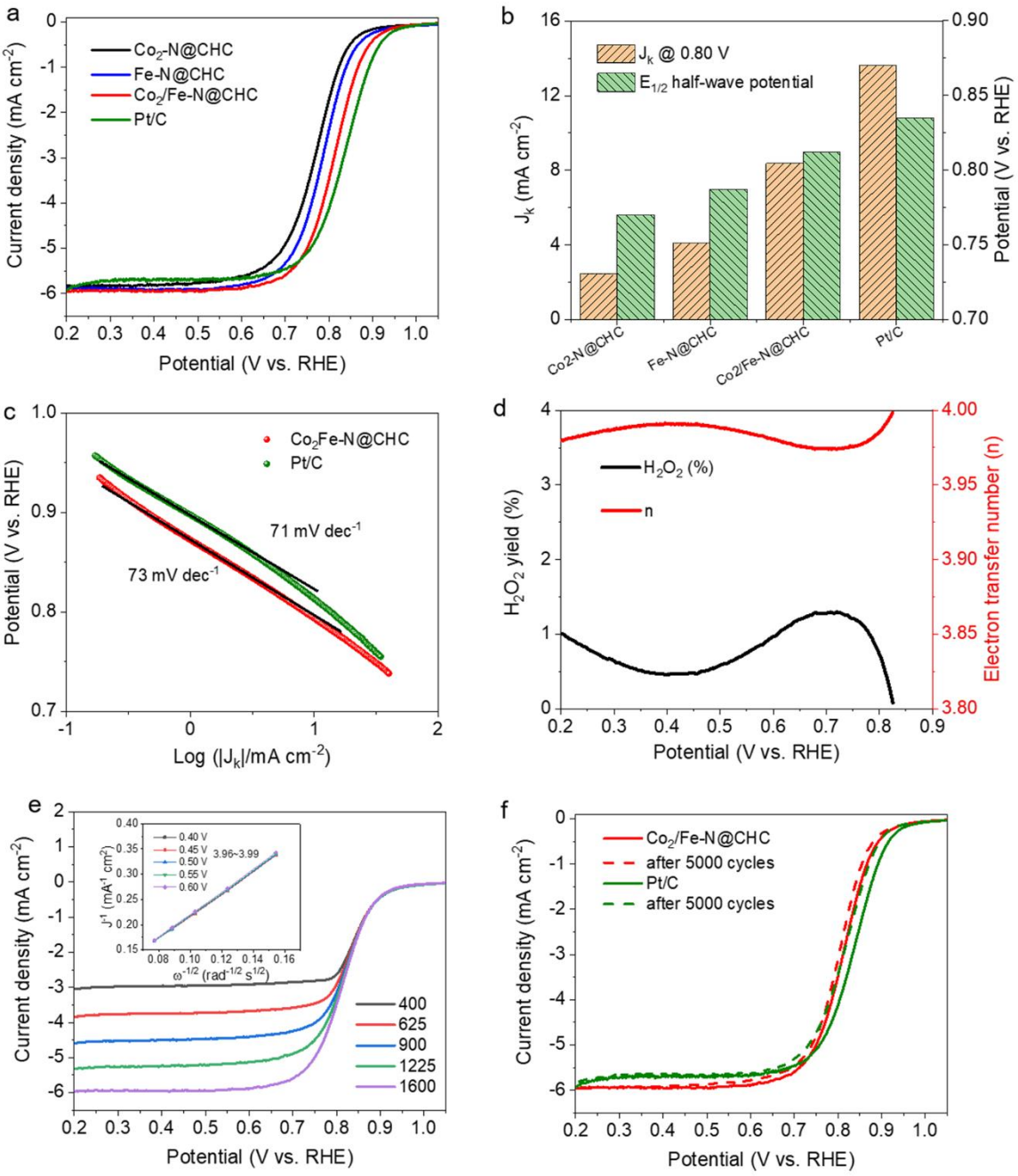

Figure S30. ORR activity and stability evaluations in O_2-staturated 0.1 M $HClO_4$. (a) Linear sweep voltammetry (LSV) curves of Co_2-N@CHC, Fe-N@CHC, Co_2/Fe-N@ CHC, and Pt/C at 1600 rpm. (b) Kinetic current density (J_k) at 0.80 V and half-wave potential ($E_{1/2}$) for these catalysts. (c) Tafel slops for Co_2/Fe-N@ CHC, and Pt/C. (d) H_2O_2 yield and electron transfer number of Co_2/Fe-N@ CHC, and Pt/C vs. potential. (e) LSV curves of Co_2/Fe-N@ CHC at different rotating rates (inset: the corresponding K-L plots and electron transfer number). (f) LSV curves of Co_2/Fe-N@ CHC and Pt/C before and after 5000 potential cycles.

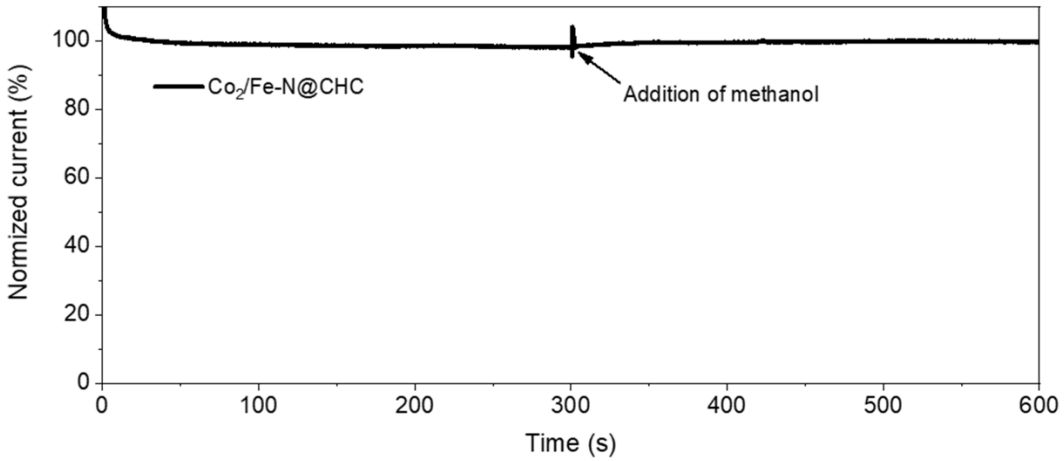

Figure S31. Chronoamperometric responses of Co_2/Fe-N@CHC at 0.7 V (vs. RHE) in O_2-staturated 0.1 M $HClO_4$ solution followed by the addition of 2 mL methanol.

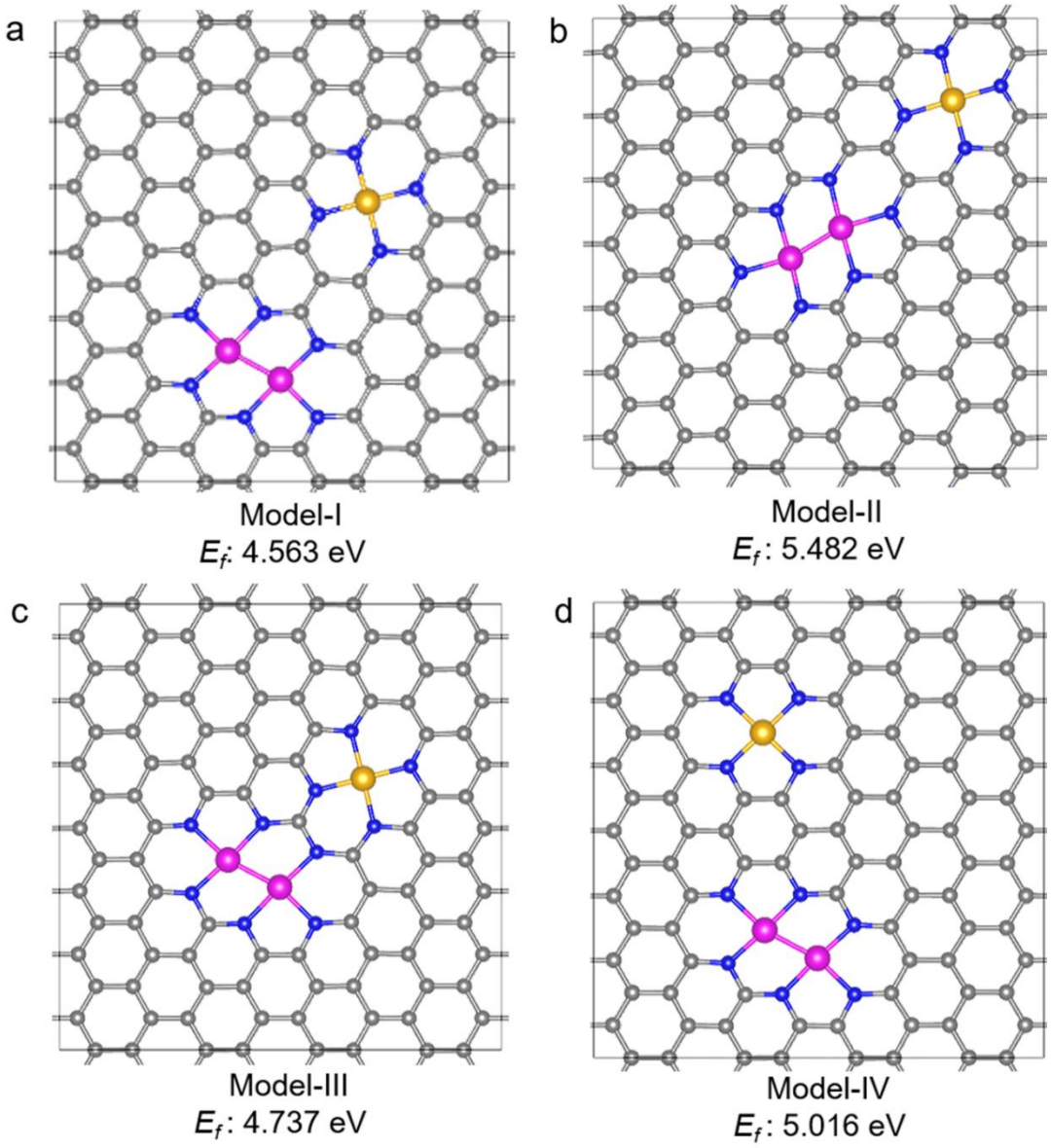

Figure S32. Possible Co_2/Fe-N_{10} structures (Top view). Their formation energies (E_f) are presented at the bottom of each model.

As shown in Figure S32, four representative models for Co_2/Fe-N_{10} systems with different arrangements and distances between Co_2-N_6 and Fe-N_4 sites were constructed. Among the four different types of atomic configurations, model-I possesses the lowest E_f. Therefore, model-I with the most energetically favourable configuration was adopted for DFT studies.

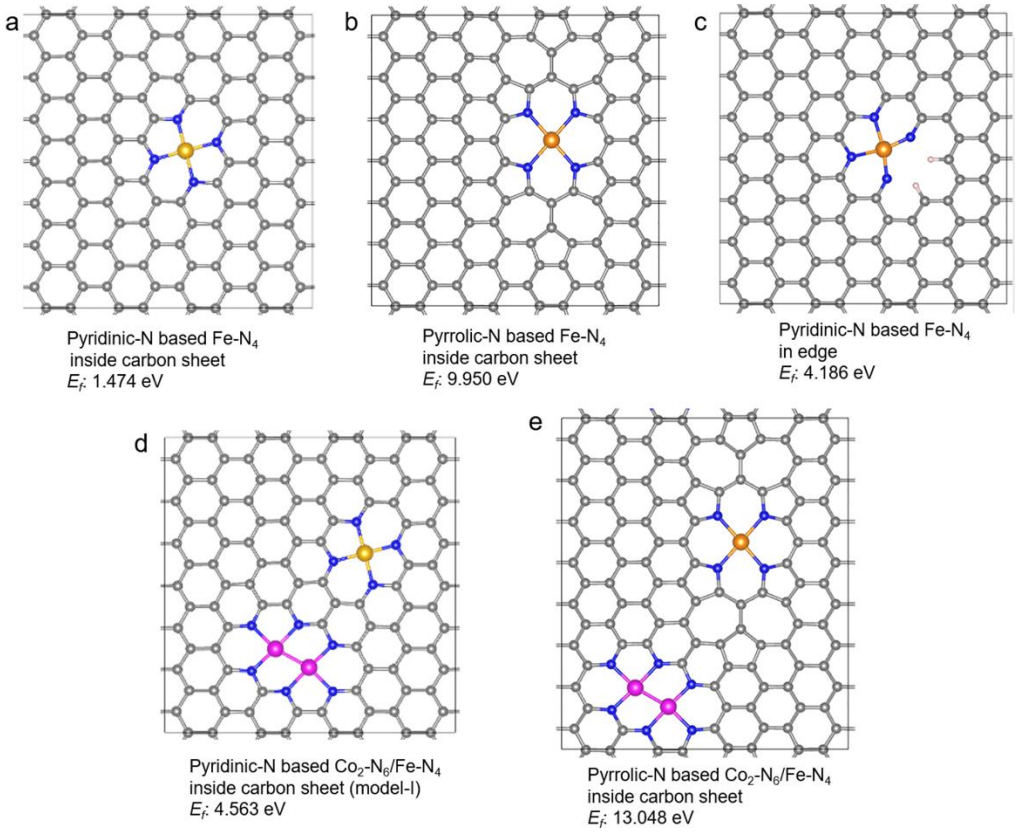

Figure S33. The top views of (a) pyridinic-N based Fe-N_4, (b) pyrrolic-N based Fe-N_4, (d) pyridinic-N based Co_2-N_6/Fe-N_4 (model-I), and (e) pyrrolic-N based Co_2-N_6/Fe-N_4 structures embedded inside carbon sheets, as well as the (c) pyridinic-N based Fe-N_4 model in edge. Their formation energies (E_f) are also presented accordingly at the bottom of each model.

As shown in Figure S33, the pyrrolic-N based Fe-N_4 and Co_2-N_6/Fe-N_4 models possess higher energy than that of our pyridinic-N based models, respectively, which means pyridinic-N based models are more energetically favourable configurations. This is also the reason why most literatures reporting single-atom catalysts and dual-atom catalysts (*Adv. Mater.* **2020**, 32, 2003134, *Nat. Commun.* **2021**, 12, 1734, *Adv. Mater.* **2020**, 32, 2004670, *Angew. Chem. Int. Ed.* **2021**, 60,14005-14012, *Adv. Mater.* **2019**, 31, 1905622, *Nat. Commun.* **2020**, 11, 2831, *J. Phys. Chem. Lett.* **2020**, 11, 1404−1410, *Angew. Chem. Int. Ed.* **2019**, 131, 2648 – 2652, *Adv. Funct. Mater.* **2021**, 31, 20065331) adopt pyridinic-N based models for their theoretical calculations. Moreover, the pyridinic-N based models in our work and the corresponding literatures are all the ones with metal active sites embedded inside the carbon sheet instead of residing at the edges that possesses higher E_f. As shown in Figure S33a, c, the Fe-N_4 model in edge has much higher E_f than that of the Fe-N_4 model inside carbon sheet. Therefore, the pyridinic-N based models embedded inside the carbon sheet are adopted in our DFT calculation.

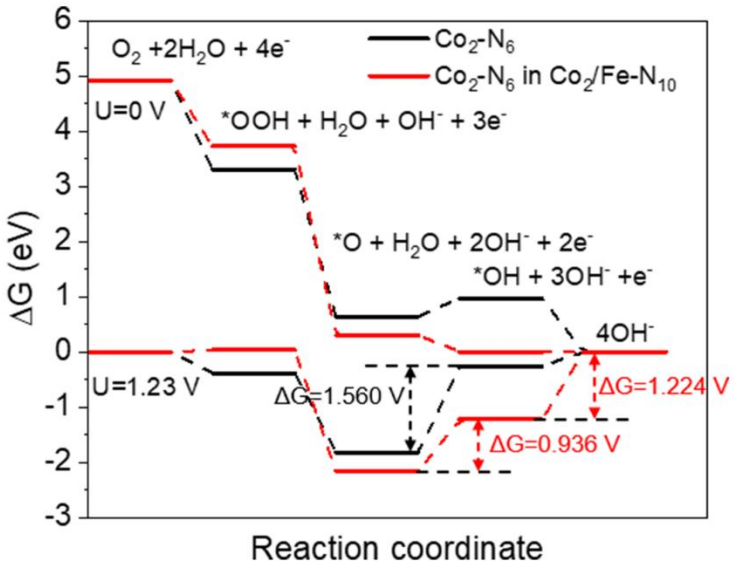

Figure S34. ORR free energy diagrams for Co_2-N_6 (black line), and Co_2-N_6 site in Co_2/Fe-N_{10} (red line) at U=0 and1.23 V along 4-electrons pathway.

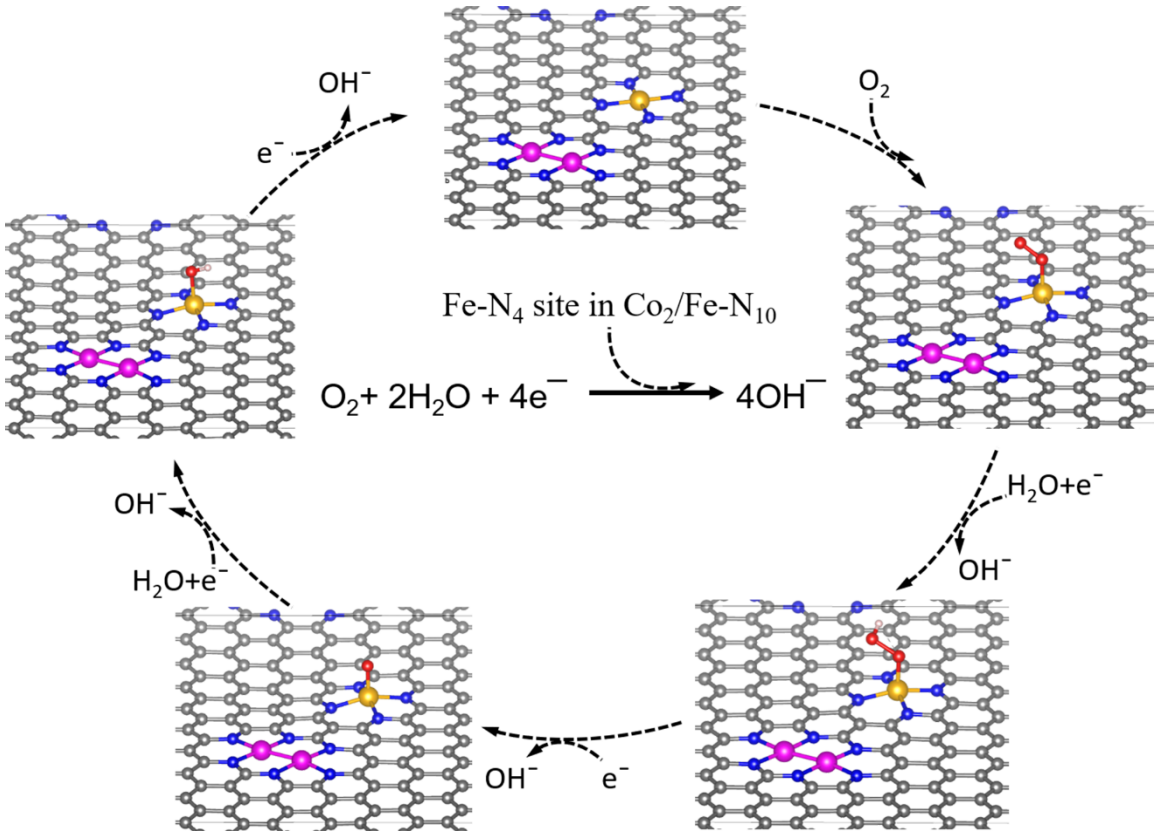

Figure S35. Illustration of ORR process on Fe-N_4 sites in the Co_2/Fe-N_{10} system.

Table S5. Bader charge states of Fe, O, and N atoms in Fe-N_4 site in Co_2/Fe-N_{10} after O adsorption, and Bader charge states of Co, O, and N atoms in Co_2-N_6 site in Co_2/Fe-N_{10} after O adsorption.

	adsorption O on Fe-N_4 site in Co_2/Fe-N_{10}			adsorption O on Co_2-N_4 site in Co_2/Fe-N_{10}			
Atom ID	Fe	O	N	Co1	Co2	O	N
Lost |e|	1.31	-	-	0.97	0.96	-	-
Obtained |e|	-	0.64	1.14 (average)	-	-	0.71	1.16 (average)

Table S6. d-bandcenter of Fe atoms in Co_2/Fe-N_{10} and Fe-N_4 systems

Atom ID	d-band-center (up)	d-band-center (down)	d-band-center (average)
Fe in Co_2/Fe-N_{10}	-2.2100	-0.3671	-1.2966
Fe in Fe-N_4	-1.5022	0.0404	-0.7365

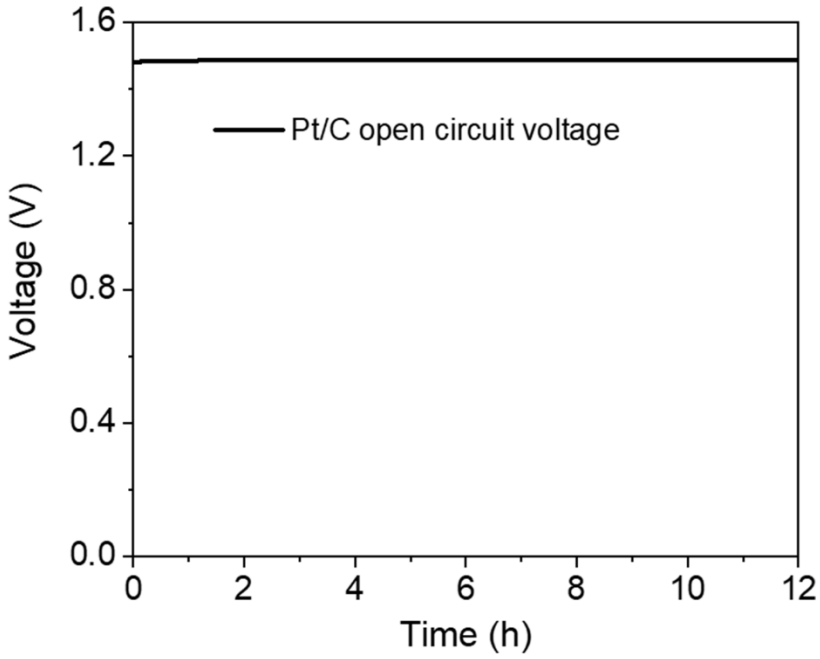

Figure S36. Open circuit voltage of the ZAB based on Pt/C.

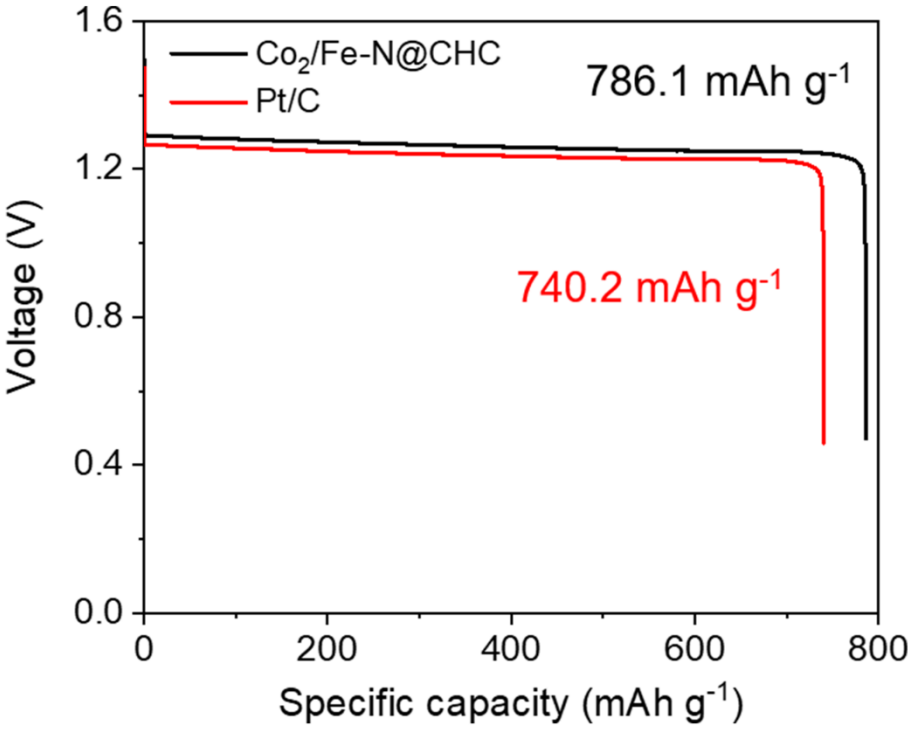

Figure S37. Long-time galvanostatic discharge curves of ZABs with Co_2/Fe-N@CHC and commercial Pt/C as cathode catalysts until complete consumption of Zn anode at a current density of 10 mA cm^{-2}. The specific capacity was normalized to the mass of consumed Zn.

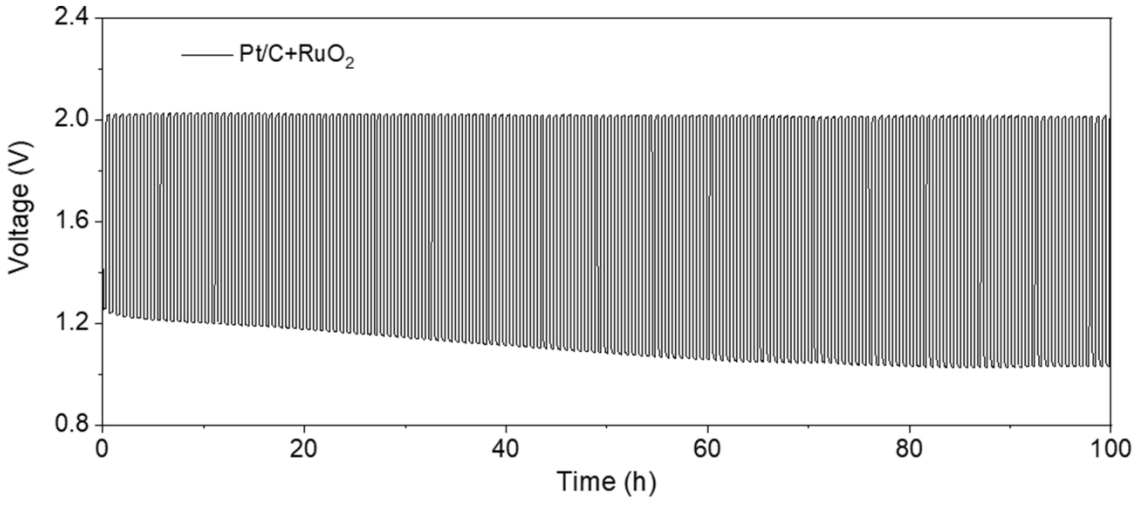

Figure 38. Galvanostatic change/discharge cycling performance of ZAB based on Pt/C+RuO_2 (with a mass ratio of 1/1) at a current density of 5 mA cm^{-2}.

Table S7. *Comparison of the performance of rechargeable Zn-air batteries reported in recent literatures.*

Air-cathode	Catalyst loading (mg cm^{-2})	Peak power density (mW cm^{-2})	Specific capacity (mAh g^{-1})	Reference
Co_2/Fe-N@CHC	2.0	232.4	786.1 @ 10 mA cm^{-2}	This work
CoSA/N,S-HCS	1.5	173.1	781.1 @ 10 mA cm^{-2}	Adv. Energy Mater. **2020**, 2002896.
S-Cu-ISA/SNC	1.0	225	735 @ 10 mA cm^{-2}	Nat. Comm. **2020**, 11, 1-11.
Fe/Ni-Nx/OC	1.0	148	712 @50mA cm^{-2}	Adv. Mater. **2020**, 2004670
Fe-N/P-C-700	3.0	133.2	723.6 @100 mA cm^{-2}	J. Am. Chem. Soc. **2020**, 142, 2404−2412
pfSAC-Fe-0.2	0.5	126.83	732 @100 mA cm^{-2}	Sci. Adv.**2019**, 5, eaaw2322.
FeCu-N-HC	1.0	209.4	-	Adv. Funct. Mater. **2021**, 31, 2006533
Fe SAs/N-C	0.5	225	636 @25 mA cm^{-2}	ACS Catal. **2019**, 9, 2158−2163
Fe/OES	0.52	186.8	807.5 @5 mA cm^{-2}	Angew. Chem., Int. Ed. **2020**, 132, 7454 –7459
Fe-SAs/NPS-HC	1.0	195	-	Nat. Comm. **2018**, 9, 1-12.
Co SAs/3D GFs	1.0	206	-	Angew. Chem., Int. Ed. **2020**, 132, 20645 – 20649

Reference

[1] G. Kresse, J. Furthmüller, *Comput. Mater. Sci.* **1996**, 6, 15.

[2] J. P. Perdew, K. Burke, M. Ernzerhof, *Phts. Rev. Lett.* **1996**, 77, 3865.

[3] G. Kresse, D. Joubert, *Phys. Rev. B* **1999**, 59, 1758.

[4] S. Grimme, J. Antony, S. Ehrlich, H. Krieg, *J. Chem. Phys.* **2010**, 132, 154104.